Solvent-free approach for processing hybrid solid electrolytes

Laurence Macray

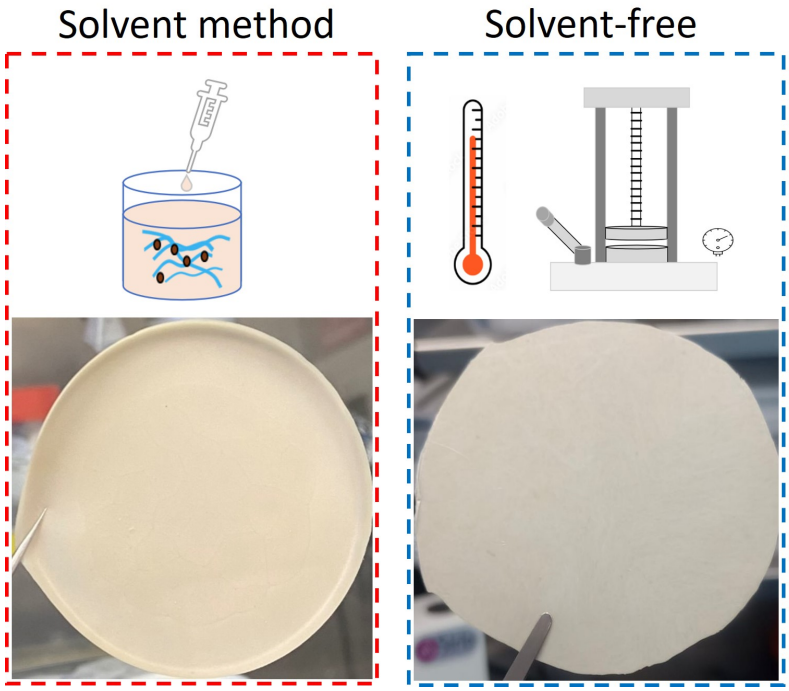

Delft University of Technology

TU Delft

Solvent-free approach for processing hybrid solid electrolytes

by

Student Name	Student Number
Laurence Macray	5584795

Thesis committee:	Prof. dr. ir. Marnix Wagemaker	TU Delft, SEE Supervisor
	Dr. Swapna Ganapathy,	TU Delft, SEE Supervisor
	Dr. Wim Bouwman,	Tu Delft, NPM2
	Shengnan Zhang,	Tu Delft, SEE Daily Supervisor
MSc:	Sustainable Energy Technology	
Institution:	Delft University of Technology	

An electronic version of this thesis is available at `http://repository.tudelft.nl/`.

TU Delft

Abstract

An all-solid-state battery represents a promising solution for overcoming current lithium-ion batteries' technological and safety limitations. However, the individual limitations of both inorganic and organic solid electrolytes hinder technological progression. Hybrid solid electrolytes hold the potential to surpass these limitations by integrating both the inorganic and organic phases. A comparative assessment was conducted between hybrid solid electrolytes produced via solvent and dry synthesis, to address potential solvent interactions during hybrid solid electrolyte production and prioritise sustainability.

At 30° C, the comparative analysis demonstrates that the dry-processed $PEO_{13}LPSC_{10}$ hybrid solid electrolyte achieves a higher ionic conductivity of 1.61×10^{-5} S/cm, exceeding that of its solvent processed counterpart, which exhibits a conductivity of 1.51×10^{-5} S/cm. Conversely, for the $PEO_{18}LPSC_{10}$ hybrid solid electrolytes, the solvent processing method leads to a higher ionic conductivity, measured at 8.37×10^{-6} S/cm, in contrast to 7.61×10^{-6} S/cm observed for the dry-processed method. Thermal analysis indicates that heating above the polymer's melting transition temperature leads to slow crystallisation in hybrid solid electrolytes using the dry method, resulting in two crystalline phases, as opposed to the single crystalline phase, which was observed using the solvent method. Both processing methods demonstrate homogeneity when comparing the top and bottom surfaces; however, an analysis of surface compositions between the two synthesis methods reveals distinct differences, as identified through X-ray photoelectron spectroscopy. Moreover, decomposition is observed in both synthesis approaches but is more significant in solvent synthesis. The chemical stability of hybrid solid electrolytes produced by dry synthesis surpasses the solvent-based method.

Further analysis through the dry method investigation reveals that an ethylene oxide to Li^+ ratio of 10:1, and a Li_6PS_5Cl ratio of 10 wt%, yield the highest ionic conductivity among all studied hybrid solid electrolytes. This combination achieves an ionic conductivity of 3.35×10^{-5} S/cm at 30° C. Additionally, adding Li_6PS_5Cl and the alkali salt lithium bis(trifluoromethanesulfonyl)imide enhances the amorphous nature and mobility of the polymer, due to a plasticising effect on the organic matrix.

Acknowledgements

After completing my Bachelor's in Chemical Engineering in 2015, I never imagined reopening my textbooks. Yet, life in rural Australia's mining sector was not my calling. Prompted by this realisation, I boarded a twenty-four-hour journey from my hometown of Perth to the Netherlands to pursue a Master of Sustainability Energy at TU Delft during the challenging times of the COVID-19 pandemic in 2021, a decision that tested me in unforeseeable ways.

I am grateful to Marnix, Swapna, and Frans for granting me the opportunity to engage in experimental work on a topic that has captivated my interest. My experience at the RID with the SEE group was awesome, made all the more enjoyable through the daily experiments and the support of the Sulfur Glovebox Team, Jeff, Zhu, Wenxuan, and Hao, who were always there to assist me. Special thanks are due to Shengnan Zhang, my daily supervisor, who, even amidst her PhD pursuits, devoted an extraordinary amount of time to guiding me. Her patience in addressing my billion questions, providing feedback, and steering me away from tangential pursuits, all with a smile, has been invaluable. Also, thanks to Joep, our exceptional teamwork significantly contributed to our focus and productivity.

To my friends and family back in Perth, especially Django, who stood by my decision and were just a phone call away, I cannot express my gratitude enough. To the community of friends, I've found here, Domaniki, Josephine, Vishnu, Ziad, Anastasis, Nicola, Alessio, thank you for maintaining my social and study balance. Lastly, a heartfelt thank you to Saoirse for helping me achieve this endeavour whilst keeping me well-fed.

Contents

List of Abbreviations

Abbreviation	Description
ACN	Acetonitrile
Al	Aluminium
ASSB	All-Solid-State Battery
CPE	Composite Polymer Electrolyte
CV	Cyclic Voltammetry
DSC	Differential Scanning Calorimetry
EO	Ethylene Oxide
EIS	Electrochemical Impedance Spectroscopy
ESW	Electrolyte Stability Window
HOMO	Highest Occupied Molecular Orbital
HSE	Hybrid Solid Electrolyte
ISE	Inorganic Solid Electrolyte
LCO	Lithium Cobalt Oxide
LFP	Lithium Iron Phosphate
LiTFSI	Lithium Bis(trifluoromethanesulfonyl)Imide
LMO	Lithium Manganese Oxide
LPSC	Lithium Argyrodite (Li_6PS_5Cl)
LSV	Linear Sweep Voltammetry
LUMO	Lowest Unoccupied Molecular Orbital
MW	Molecular Weight
NMR	Nuclear Magnetic Resonance
PEG	Polyethylene Glycol
PEO	Polyethylene Oxide
PET	Polyethylene Terephthalate
PTFE	Polytetrafluoroethylene
RT	Room Temperature
SPE	Solid Polymer Electrolyte
SS	Stainless Steel
THF	Tetrahydrofuran
T_g	Glass transition temperature
T_m	Melting transition temperature
XPS	X-ray Photoelectron Spectroscopy

1

Introduction

Since their introduction in 1991, lithium-ion batteries (LIBs) have become a significant part of everyday life, profoundly influencing the electronics sector. Their application has expanded to stationary storage and electric vehicles, driven by their high energy content and rechargeability [1]. Furthermore, global demand for LIBs is exploding and is expected to increase by 14 times by 2030, indicating their vital role in the energy transition [2]. Despite this, current safety considerations must be addressed, highlighted by a recent incident where a fire involving the Fremantle Highway off the coast of the Netherlands raised major safety concerns [3]. This incident, involving a cargo ship carrying 498 electric vehicles, underscored the risks associated with the highly flammable organic liquid electrolytes in these batteries.

From a technical standpoint, current LIBs, which use graphite as the anode material, are nearing their theoretical specific capacity limit of approximately 372 mAh/g [4]. An all-solid-state battery (ASSB) represents a promising solution, aiming to address the technological and safety limitations of current LIBs by substituting the organic electrolyte with a solid one. Moreover, ASSBs offer the potential for increased energy density due to bipolar stacking, allowing for denser, more efficient packing and reducing reliance on inactive [5]. Yet, the performance of the solid-state electrolytes has to surpass that of their liquid counterparts, highlighting a crucial area of research. The primary types are inorganic solid electrolytes (ISE) and organic solid polymer electrolytes (SPE). Each type has its own disadvantages; for instance, ISE are known for their high ionic conductivity but suffer from poor mechanical properties and interfacial stability with electrodes [6]. SPE, on the other hand, offer better flexibility and ease of processing but typically exhibits lower ionic conductivity than ISE [7]. To overcome these limitations, the development of hybrid solid electrolytes (HSE) has gained momentum. HSEs combine the high ionic conductivity of ISE with the mechanical stability and favourable interfacial properties of SPE, addressing the downfalls of both ISE and SPE.

This report aims to explore two current processing methods of the HSE, PEO-LiTFSI-LPSC (polyethylene oxide, lithium bis(trifluoromethanesulfonyl)imide)(LiTFSI), and lithium argyrodite (Li_6PS_5Cl))(LPSC)), focusing on dry and solvent approaches. This investigation is inspired by the previous study, by [8] using a solvent approach to synthesise a PEO-LiTFSI-LPSC HSE, which demonstrated that the interfacial resistance of LPSC was a bottleneck in lithium-ion conduction and prevented the formation of a unified conducting phase between inorganic and organic phases. Furthermore, introducing ionic liquids lowers the diffusion barrier and thus facilitates efficient ion conduction pathways between organic and inorganic phases. A dry method synthesis presents a promising alternative to bypass potential solvent interactions and the necessity for additional additives, such as ionic liquids, by providing a more favourable diffusion pathway, thereby addressing sustainability concerns by reducing waste and processing costs. Building on the foundation laid by [8], this study seeks to further the understanding of the interplay between synthesis methods and the resultant electrochemical performance of the most studied HSEs produced by the TU Delft Battery team. The focus will subsequently shift to exploring various LPSC and LiTFSI compositions to see which provides better electrochemical performance using dry synthesis.

This report is structured as follows: The remaining sections of Chapter 1 will conduct a comprehensive literature review. Chapter 2 outlines the methodology and experimental aspects of the report. Next, in Chapter 3, two studies are introduced, the first of which comparatively addresses two methods of processing HSE using dry and solvent approaches. A further investigation follows this to see how the active fillers LiTFSI and LPSC influence the performance of the HSE using dry synthesis. Finally, in Chapter 5, conclusions and recommendations are discussed.

1.1. All-Solid-State batteries

To understand the evolution of an ASSB, a LIB is first explored. As shown in figure 1.1 , a LIB cell consists of several key components. Starting from the left of figure, the cell features a current collector (usually aluminium foil) with a high voltage cathode attached, commonly made from transition metal oxides like lithium iron phosphate (LFP), lithium cobalt oxide (LCO), or lithium manganese oxide (LMO) [1][9]. In the centre, a microporous separator soaked in a liquid electrolyte (a lithium salt in an organic solvent) enables lithium ions to migrate by a vehicular transport mechanism between the anode and cathode whilst also serving as a physical barrier to prevent short circuits. Lastly, on the right presents the anode, typically graphite or amorphous carbon binding to copper foil current collector [1].

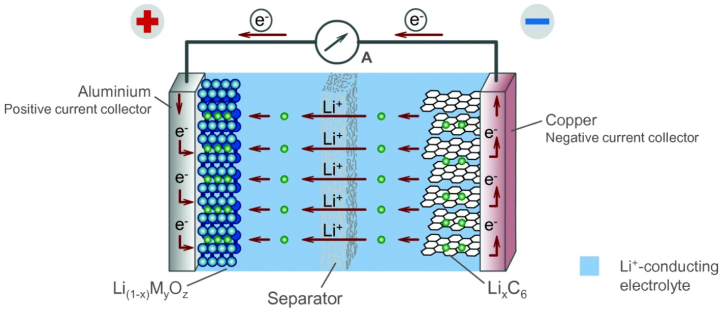

Figure 1.1: LIB battery components during discharge process [1].

The flammability and fluid nature of the of organic liquid electrolytes in LIB enhances safety risks, such as internal short circuits leading to fires if containment is lost. Consequently, each unit cell is sealed to contain the liquid electrolyte, as illustrated in figure 1.2 a). As a result, this requires adding many inactive parts, limiting the energy density and increasing production costs [5].

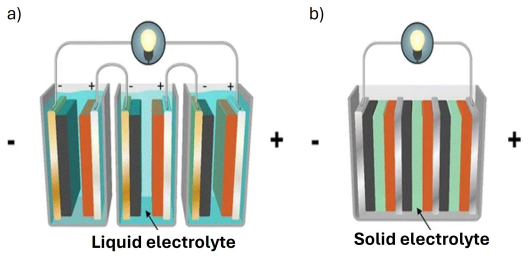

Figure 1.2: a) Structure of a LIB b) Structure of an ASSB [10].

Transitioning to an ASSB addresses these limitations through the solid electrolyte, either an ISE, SPE or HSE, that serves as a physical separator between the electrodes and Li-ion conduction medium, thus eliminating the need for flammable organic electrolytes. Moreover, each unit cell in an ASSB does not require sealing since there is no risk of electrolyte leakage. This opens up possibilities for more efficient cell configurations, such as bipolar stacking, allowing for denser packing and reducing the reliance on inactive materials, which lead to an increase in energy density [5]. This concept is illustrated in the figure 1.2 b). Despite its potential benefits, an ASSB is incompatible with the high-voltage cathodes and graphite anodes used for LIB, requiring further technological development [11].

Shifting the focus to the operating principle of an ASSB, it remains fundamentally the same as a LIB during the charge and discharge phases. This similarity facilitates a smoother transition to ASSB technology. Starting at a fully charged state (right of figure 1.1) when the lithium is stored within the graphite layers. During the discharge phase, the lithium in the anode undergoes oxidation, losing an electron to become a lithium-ion, as described by the half-reaction equation 1.1.

$$Li_xC_6 \longrightarrow C_6 + Li^+ + e^- \tag{1.1}$$

These lithium ions then migrate through the electrolyte and separator towards the cathode while simultaneously, the electrons travel through the external circuit. This separation of charge is what generates

the electrical current. When the lithium ions reach the cathode, they are reduced and intercalate into the layers of the cathode material, as identified by the half-reaction equation 1.2

$$Li_{(1-x)}MO_2 + Li^+ + e^- \longrightarrow LiMO_2 \tag{1.2}$$

Moreover, the overall charge and discharge reactions are described by the equation 1.3

$$Li_{(1-x)}MO_2 + Li_xC_6 \longrightarrow C_6 + LiMO_2 \tag{1.3}$$

1.1.1. Ionic conduction in solid-state electrolytes

Although the fundamental operating principles during cycling remain similar, the diffusion mechanisms of lithium ions differ in solids and are explained below.

Conduction in an ISE

Ionic diffusion in a crystal structure occurs through a hopping diffusion mechanism, where an ion jumps from one position to another. Depending on the material's structure, this process can occur in one, two, or three dimensions. There are three primary mechanisms of ion migration: vacancy diffusion, direct interstitial, and correlated intrinsically [6]. These three forms of ion migration are illustrated by figure 1.3.

The first example of ion migration, vacancy diffusion involves an ion migrating to a vacancy, an empty lattice site or a defect in the crystal structure. This process leaves behind a new vacancy that another ion can occupy, facilitating ion movement across the crystal lattice. Meanwhile, direct interstitial migration occurs as an ion migrates from one interstitial site to another. Finally, correlated migration, also called the knock-on mechanism, occurs when an interstitial ion displaces a lattice ion into an interstitial space, thereby promoting ion migration within the lattice [12].

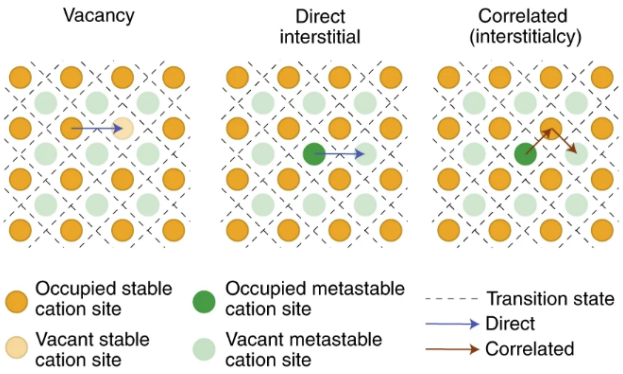

Figure 1.3: Diffusion mechanisms in a crystalline lattice [6].

Additionally, central to understanding these diffusion mechanisms is the concept of ion mobility (μ), which is expressed by the Nernst Einstein relation in equation 1.4

$$D = \mu k_B T \tag{1.4}$$

In this equation D is the diffusion coefficient in units of, μ is the ion mobility, k_B is the Boltzmann constant, and T is the temperature. Subsequently, the ionic conductivity σ of a material, which defines the ability to conduct electrical charge, can be explored through the understanding of diffusivity, which is represented by 1.5

$$\sigma = \mu \cdot c \cdot z \tag{1.5}$$

Here, μ is the ion mobility, c is the charge carrier concentration, and z is the charge per carrier. To further highlight the relationship between the diffusivity and conductivity, equation 1.4 and equation 1.5 can be combined to form equation 1.6.

$$\sigma = \frac{D \cdot c \cdot z}{k_B T} \tag{1.6}$$

Further more, ionic conductivity is a temperature-dependent mechanism as identified by equation 1.6. This is governed by activation energy (E_a, which is the minimum amount of energy required for a reaction to occur, but in this case, for an ion to hop (migrate), it can be expressed by the Arrhenius Equation 1.7.

$$\sigma(T) = \sigma_0 . exp^{-\frac{E_a}{k_B T}} \tag{1.7}$$

where $\sigma(T)$ denotes the ion conductivity, σ_0 represents the pre-exponential factor, E_a is the activation energy, k_B denotes Boltzmann's constant, and T is the temperature.

Conduction in a SPE
Ionic conduction in a SPE is facilitated through the segmental motion of the polymer chains and the number of mobile ions, as described by equation 1.5. The onset of this segmental motion occurs above the glass transition temperature (T_g), this is the point where the polymer transitions from a hard, glassy material to a soft, rubbery state. Subsequently, the segmental motion generates free volume near the mobile chain segments, providing the necessary space for ions to hop, driven by an electric field [13].

Unlike an ISE , the temperature dependence of ionic conductivity is not described by the Arrhenius Equation. In contrast, above the glass transition temperature T_g, the temperature-dependent conduction of the lithium ions follows the Vogel-Tamman-Fulcher (VTF) model described by the equation 1.8.

$$\sigma(T) = \sigma_0 . \exp\left(-\frac{B}{k_B(T - T_0)}\right) \tag{1.8}$$

In this equation, $\sigma(T)$ represents the ionic conductivity, σ_0 is the pre-exponential factor, k is the Boltzmann constant, B is the pseudoactivation energy, and T_0 is the Vogel temperature. The Vogel temperature T_0 is generally set 50 °C below T_g [14] .

Conduction in a HSE
Similar to both ISE and SPE, the ionic conductivity of a HSE is expressed by equation 1.5. However, there are two competing ion propagation mechanisms in the HSE system, one through the ISE and the other through the SPE [15]. Ideally, the ionic conduction of lithium ions should form a unified conductive network, allowing ions to diffuse between inorganic and organic counterparts.

As a result, there is yet to be a definitive method for interpreting the temperature dependence in HSE. One study introduced two Arrhenius equations to capture the distinct conductivity behaviours at temperatures above and below the melting transition temperature (T_m) [16]. Conversely, another research effort utilised a single Arrhenius plot to assess the temperature dependencies on ionic conductivity [8]. Further studies have indicated that incorporating inorganic phases into the SPE at ratios exceeding 60 wt% alters the conduction mechanism to follow an Arrhenius model. However, below this threshold, the VFT model is applied [14]. Lastly, in the case of [17], two activation energies for high and low-temperature regions were determined; however, there needs to be more mention as to the model used.

1.1.2. Hybrid solid electrolytes

A HSE, also known as a composite polymer electrolyte (CPE), incorporates either an inorganic filler in a SPE or a SPE in an ISE [18]. The following section will first introduce the ideal metrics for a HSE. Afterwards, the components of an HSE will be divided into two parts: the ISE, focusing on the LPSC system, and the SPE, concentrating on the PEO-LiTFSI system. The final part will discuss integrating these two systems into the PEO-LiTFSI-LPSC, HSE system.

1.1.3. Ideal metrics for a HSE

- **High bulk Ionic Conductivity:** This characteristic is often referred to as the King metric for solid electrolytes. High ionic conductivity, aiming to be comparable to liquid organic electrolytes, has been a primary driver of extensive research. An electrolyte with a high ionic conductivity enables optimal battery performance at practical power densities, which is highly sought after for electric vehicles (EVs) and many other electronic applications. As was pointed out previosly, ionic conductivity is temperature-dependent, and the operating window of LIB can range between -20 °C and 60°C [19]. Consequently, this highlights the importance of solid electrolytes' ability to meet the charge transfer kinetics across a wide temperature range..

- **Thermal stability:** The same temperature range mentioned above highlights the crucial aspect of thermally stable electrolytes.
- **Mechanical stability:** Mechanical stability is critical for maintaining the integrity of the solid electrolyte and the electrodes. During battery operation, active materials can undergo significant volume changes, compromising the electrolytes mechanical stability. This can lead to fractures, loss of contact, or uneven electrode deposition, both of which can severely impact battery performance [6].
- **Low interfacial resistance and enhanced interface stability:** To ensure high lithium-ion conduction while remaining electronically insulating, it is crucial to achieve not only low interfacial resistance but also enhanced interface stability. Failure to meet these criteria can lead to high internal resistance and high overpotentials during cycling, which can reduce the battery's efficiency and lifespan, and introduces additional safety risk [20].
- **Lithium dendrite suppression:** Initially, the solid electrolyte's rigid mechanical structure was believed to be more resistant to dendrite formation. However, large volume changes of electrodes during cycling can lead to contact loss and impose inhomogeneous plating and stripping of the lithium [6].
- **Wide electrochemical stability and appropriate electrode compatibility:** The electrolyte stability window (ESW) is an important parameter in defining the performance of batteries. It is defined as the voltage difference between the oxidation and reduction potentials. Additionally, this window represents the energy difference between the lowest unoccupied molecular orbital (LUMO) and the highest energy occupied molecular orbitals (HOMO) [21]. A wide ESW, greater than 4.2 V vs Li/Li+, allows for high energy density applications. The pairing of solid electrolyte materials is important, with HOMO and LUMO levels needing to align with the electrochemical potentials of the of the anode and cathode materials to avoid decomposition [21].
- **Environmental sustainability:** This aspect requires greater attention, especially after the European Union introduced a new directive in June 2023 to improve battery waste management throughout their lifecycle. This is essential, given the expected increase in battery demand by over fourteen times from current levels by 2030 [22]. Furthermore, the directive aims to establish a circular economy focusing on environmentally sustainable battery design and end-of-life solutions.
- **Low processing costs:** Ensuring the affordability of solid electrolytes is key to facilitating their integration into ASSB.

1.1.4. LPSC system

Lithium argyrodites is an ISE with the formula Li_6PS_5X (X: Cl, Br, I), which is a sufide electrolyte that has gained considerable interest since their discovery [23]. A desirable feature of this type of electrolyte is the high room temperature conductivities, shown to be in the range of 10^{-3} S/cm, comparable to liquid electrolytes [24]. Structurally, Li_6PS_5X exhibits a cubic F43m symmetry and within this structure, lithium ions move in three distinct ways, as revealed by molecular dynamics [25]. Two of these involve short-range jumps, characterised by back-and-forth transitions occurring at 48h-48h sites and intracage transitions feature transitions between 48h sites. Additionally, intercage jumps represent long-range movements between the four cages of the unit cell [25]. Furthermore, LPSC ion conduction obeys the Arrhenius behaviour [26].

Despite its exceptional ionic conductivity, LPSC presents many potential challenges, specifically its hydrolysis stability and electrochemical stability. The hydrolysis stability of LPSC can be understood through equations 1.9 to 1.11 [27].

$$Li_6PS_5Cl + 6H_2O \rightarrow LiCl + Li_3PO_4 + 5H_2S + 2LiOH \tag{1.9}$$

$$2LiOH + CO_2 \rightarrow Li_2CO_3 + H_2O \tag{1.10}$$

$$Li_6PS_5Cl + 4H_2O + 2O_2 \rightarrow LiCl + Li_3PO_4 + 4H_2S + Li_2SO_4 \tag{1.11}$$

Due to this instability, production of LPSC is carried out in a controlled atmosphere. This requirement not only restricts its processability but also escalates the production costs. Moreover, this emphasises the need to develop a more stable structure. As further highlighted by [28], in this study, it was reported that a 10-minute exposure alone to a 65% humidity atmosphere led to a reduction in the ionic conductivity of LPSC by approximately 13.3%, decreasing from 1.8 mS/cm to 1.56 mS/cm [28].

Shifting to the chemical stability of LPSC, [29] applied density functional theory (DFT) to determine the ESW. It was found to be exceedingly narrow (0.3 V), and stable in the range of 1.71 V to 2.01 V vs. Li^+/Li. This range corresponds to the phase equilibria during reduction at 1.71 V, forming P, Li_2S, LiCl, and oxidation at 2.01 V, forming Li_3PS_4, LiCl and S [29]. However, an experimental study by [30] revealed LPSC as having a much wider ESW of 1.25 V, remaining stable in the range of 1.25 V to 2.50 V vs. Li^+/Li. Investigating the redox activity of LPSC,[31] revealed two oxidation peaks at 2.6 V and 3.0 V during a positive sweep through cyclic voltammetry (CV), corresponding to the formation of S and P_2S_5 as oxidised products. Conversely, a negative sweep indicated two reductive peaks at 2.0 V and 1.1 V corresponding to Li_2S and Li_3P respectively. [31]. Moreover, the associated oxidation and reduction reactions are represented by equations (1.12) and (1.13):

$$Li_6PS_5Cl \longrightarrow LiCl + \frac{1}{2}P_2S_5 + \frac{5}{2}S + 5\,Li^+ + 5\,e^- \quad \text{(ox)} \tag{1.12}$$

$$Li_6PS_5Cl + 8\,Li^+ + 8\,e^- \longrightarrow LiCl + Li_3P + 5\,Li_2S \quad \text{(red)} \tag{1.13}$$

Another limitation of LPSC, similar to other inorganic solid electrolyte compounds, is the compromised contact between electrolytes and electrodes in cell configurations, attributable to inadequate mechanical stability during cycling. Not only this, but lithium dendrites can form on the interphase between the anode and electrolyte, deteriorating the battery by penetrating the electrolyte through its grain boundaries or voids within the bulk material [32]. Additionally, however, applying high pressures can lead to the deformation of electrodes such as lithium, compromising the overall stability of the battery system through short circuits.

Moreover, measuring and using LPSC for electrochemical testing is challenging. As LPSC is powdered, it must be pelletised. This means applying exceptionally high pressures up to 300 MPa [33]. Consequently, measurements must be undertaken within customised solid-state laboratory cells to ensure close electrode contact. Adding to this challenge, an investigation of Br^-/S^{2-} site disorder in Li_6PS_5Br concluded that ionic conductivity decreases with increasing applied pressure, indicating that pressure must be carefully managed to optimise the performance of Li_6PS_5X, which may have previously been overlooked [34].

1.1.5. PEO-LiTFSI system

PEO is a semi-crystalline polyether compound consisting of repeating ethylene oxide (EO) units, as represented by the formula $H-(O-CH_2-CH_2)_n-OH$. Within this polymer are both amorphous and crystalline regions, where the amorphous regions provide flexibility, and the crystalline regions offer structural stability. PEO is typically referred to as such, if the MW of the polymer is greater than 20,000 g/mol, below this threshold, the polymer is known as polyethylene glycol (PEG) [35]. The polymer's properties, including its melting transition temperature (T_m), which ranges from approximately 65-70°C and its T_g at around -60°C and crystallinity of 75-80%, can vary depending on its MW [36][37][38].

The formation of the SPE occurs through the addition of lithium salt, in this case, LiTFSI, which has two primary roles in the system: to provide lithium-ion charge carriers and to suppress crystallisation, acting as a plasticiser through the addition of the bulky TFSI ion [39]. The PEO-LiTFSI system has emerged as particularly promising. This preference is attributed to its superior ionic conductivity compared to other SPE, with values of 10^{-5} S/cm, a relatively wide ESW up to 3.8 V versus Li/Li+, and high mechanical stability, which allows for low interfacial resistance between the electrolyte and electrode [40][41]. Not only does the PEO-LiTFSI system demonstrate this, but it also enables the potential for large-scale fabrication due to the ease and simplicity associated with processing thin electrolyte films[42].

In the SPE system, the dissociation of LiTFSI is facilitated by the PEO's Lewis base character (the ether oxygen), which assists in the dissociation of LiTFSI through coordination with the lithium ions. The movement of lithium ions in a PEO-LiTFSI system occurs via coordination with the ether oxygen atom of the monomer. This coordination process involves both breaking and forming bonds between lithium and oxygen. Consequently, conduction occurs either through intrachain or interchain hopping, facilitated by the segmental motion of the polymer chains as depicted in figure 1.4 [43].

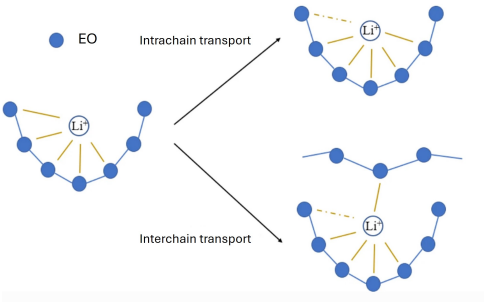

Figure 1.4: Lithium ion movement in PEO-LiTFSI SPE system [43].

To enhance ionic conductivity at room temperature in PEO-LiTFSI systems, achieving a high amorphous content and a low T_g is essential. However, the addition of LiTFSI serves as a plasticiser, which leads to a lower melting transition temperature T_m of PEO. Interestingly, it also paradoxically increases the T_g or PEO, an effect attributed to the interactions between LiTFSI and PEO chains, which can restrict segmental motion of the polymer chains despite the plasticising effect [44].

Despite this, the ionic conductivity of PEO-LiTFSI systems has been shown to increase with increasing salt concentrations, i.e., lower molar ratios of EO: Li^+. Furthermore, research has identified a crystallinity gap ideal for ambient temperature applications in which the SPE maintains an amorphous structure, thus increasing the ionic conductivity. A study analysed a PEO-LiTFSI system by incorporating low MW PEG (3.9×10^3 g/mol) and LiTFSI, with a crystallinity gap occurring between 8:1 and 12:1 ratios, even when subjected to -5°C for two months, no crystallinity was detectable [45]. In the same 8-12 EO:Li^+ ratio region, using higher MW PEO, this time at 5×10^6 g/mol, a different phenomenon occurred. Here, the increase in polymer chain length influenced the crystallisation behaviour by leading to two coexisting PEO phases: a 6:1 crystalline complex and an 11:1 amorphous phase [40]. Moreover, a peak conductivity was observed at an EO: Li^+ ratio of 10:1, with a conductivity greater than 3×10^{-5} S/cm, indicating how specific EO: Li^+ ratios can optimise the SPE phase structure for enhanced ionic conductivity [40].

Another important finding from [40] is that the PEO-LiTFSI system has a very slow re-crystallisation period; for this reason, samples that had undergone pre-heat treatment showed higher conductivities compared to their counterparts that had been recrystallised at -10°C for 72 hours. Not only does slow re-crystallisation occur in these concentrated ratios, but in a very dilute salt concentrations (50:1), it is not as significant but still occurs [46]. Despite of this, study by [47] investigating an EO: Li^+ ratios of 10, 12, 15 and 20:1 reported that ionic conductivity measurements were taken two hours after pre-heating cells to 70°C, which was above the T_m of the PEO 3.0×10^5 g/mol [48]. This makes it challenging to establish if these findings accurately reflect the system's equilibrium state. This highlights the need for standardised testing conditions to compare ionic conductivity results across different studies accurately.

1.1.6. PEO-LiTFSI-LPSC system

The addition of LPSC to PEO-LiTFSI completes the HSE system. In the PEO-LiTFSI-LPSC system, competing lithium ion conduction networks exist via the PEO-LiTFSI and another through LPSC, with the latter becoming dominant beyond a percolation threshold. Using a solvent, synthesis [16] revealed that increasing the concentration from 1 wt% to 40 wt% at an EO:Li^+ ratio of 20:1, using PEO with a MW of 4.0×10^5 g/mol, resulted in improved ionic conductivity from 5.0×10^{-6} S/cm to 5.9×10^{-5} S/cm at 30°C. This improvement, though, was not attributed to a percolation network of LPSC, but rather to the active filler's ability to kinetically inhibit PEO crystallisation, effectively reducing its crystallinity from 66.5% to 44.5% an enhancing the segmental motion of the PEO-LiTFSI.

In an ideal PEO-LiTFSI-LPSC system, a single unified ion conduction would occur, allowing for the HSE to achieve ionic conductivities comparable with liquid electrolytes. This would only be possible if the diffusion barrier between the organic-inorganic phases were favourable or if a percolation network through the LPSC was created. To further understand the organic-inorganic interface as a potential bottleneck for lithium-ion transport, [8], produced a HSE, using PEO 6.0×10^5 g/mol with 10 wt% LPSC and an EO:Li^+ ratio of 18:1. It was observed that the incorporation of an ionic liquid methyl-1-

propylpiperidinium bis(trifluoromethylsulfonyl)imide, wet the polymer-inorganic interface, which allowed for a reduction in the diffusion barrier and high ionic conductivity of 2.47×10^{-4} S/cm at room temperature (RT). The enhancement the ionic liquid provides is depicted through a diagrammatic representation, as illustrated in figure 1.5. This figure highlights two key aspects: a) The PEO-LiTFSI-LPSC system experiences a tortuous conduction path through the SPE when LPSC is introduced, indicating impedance to ion transport. Conversely, b) illustrates an efficient ion conduction path facilitated by the lower diffusion barrier between the organic-inorganic interface once an ionic liquid is added.

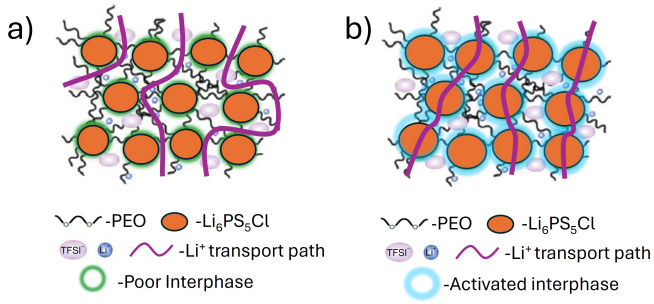

Figure 1.5: Lithium ion conduction in PEO-LiTFSI-LPSC system a) without methyl-1-propylpiperidinium bis(trifluoromethylsulfonyl)imide b) With methyl-1-propylpiperidinium bis(trifluoromethylsulfonyl)imide [8].

HSE processing methods

There are two primary methods for preparing HSE on a laboratory scale, solvent casting and thermo-compression (dry method), and a comparison is summarised in table 1.1.

Table 1.1: Comparison of Solvent Casting and the dry method Processes for HSE.

Aspect	**Solvent Casting**[8][16]	**Dry processing**[43]
Process Steps	Mixing a lithium salt and inorganic filler in an organic solvent, stirring for 24 hours, then casting on a non-stick surface. Initial drying is for 24 hours, with further drying under reduced pressure for 48 hours.	Involves manual grinding or ball milling inorganic fillers with the polymer, then heating and pressing the mixture between foil sheets.
Processing Time	Extended processing times due to 24-hour stirring, plus 72 hours for drying.	Quicker and more efficient, with no drying time required, significantly shortening the production time.
Solvent Use	Organic solvents like tetrahydrofuran (THF) or acetonitrile (ACN) are used but not recovered, leading to waste.	No use of organic solvents, eliminating waste and the need for solvent recovery.
Homogeneity of HSE Membrane	Enhanced homogeneity from thorough mixing and dispersion of the inorganic filler and dissociation of lithium salt.	Potential issues with uniformity could impact the quality and performance of the HSE membrane.
Influence on Electrochemical Performance	Possible instability with the inorganic phase and risk of inaccurate ionic conductivity readings due to residual solvent.	No risk of residual solvent affecting electrochemical performance, likely leading to more reliable measurements.
Environmental Impact	Significant solvent waste, considering a HSE produced by [8], results in 5.73g of solvent waste per g of HSE produced, affecting cost and sustainability if the solvent is not recovered.	Minimal waste production due to the absence of solvents, enhancing environmental benefits and reducing costs.

2
Methodology

This chapter highlights the materials and methods used for processing HSE systems and provides an overview of the types of characterisation techniques that were explored.

2.1. Sample preparation

2.1.1. Dry synthesis

To prevent moisture interaction with the samples, all hybrid solid electrolytes (HSE) were prepared in an argon atmosphere containing less than 1 ppm of H_2O and O_2. Commencing the process, 1 µm fine powder of Li_6PS_5Cl (NEI Corporation) and LiTFSI (ELYTE Innovations) were weighed and hand-ground using a pestle and mortar, for over 15 minutes. Following this, PEO (Sigma-Aldrich, M_w=600,000 g/mol) was gradually introduced in 0.05g segments and ground for 15 minutes. The specific amount of LiTFSI in the SPE was calculated based on the stoichiometric ratio of ethylene oxide to lithium (EO:Li^+), with ratios (10:1, 13:1, or 18:1). Additionally, the ratio of Li_6PS_5Cl was adjusted to be 10% to 30 wt% of the total mass, as detailed further in table 2.1. Furthermore, the naming convention used for the HSE concerns the $(EO:Li^+)$ and LPSC ratio, where 'x' corresponds to the $(EO:Li^+)$ ratio and 'y' to the LPSC ratio in PEO_xLPSC_y.

Following the preparation of the electrolyte mixture, the resulting dough was placed between two Polytetrafluoroethylene (PTFE) sheets, accompanied by a 150 µm spacer, and positioned within a two-plate stainless steel assembly. This assembly is then heated on a hotplate set to 110°C. Once the set-point temperature is reached, the assembly remains in place for 10 minutes. Afterwards, it is removed and subjected to compression under a hydraulic press at 35 bar. Following compression, the dough, now flattened into a membrane, is folded to enhance mixing. The heating, compression, and folding process is repeated three times to ensure uniformity. Finally, the assembly is left to cool under continuous compression for 24 hours. The extended cooling period under continuous compression allows the membrane to cool slowly and uniformly, minimising exposure to external temperatures. See figure 2.1 for a schematic representation of the entire methodology.

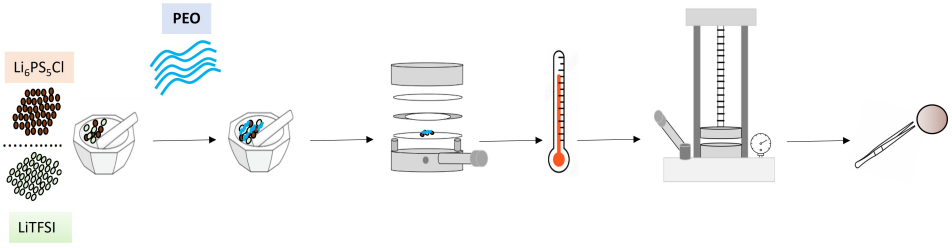

Figure 2.1: Schematic representation of the dry method used to synthesise HSE.

Table 2.1: Compositions of HSE.

LPSC Content (wt%)	Molar Ratio EO: Li^+	PEO (mg)	LiTFSI (mg)	LPSC (mg)
10	10	314.07	204.69	57.64
	13	345.53	173.23	57.64
	18	380.86	137.90	57.64
20	10	279.17	181.95	115.28
	13	307.14	153.98	115.28
	18	338.54	122.58	115.28
30	10	244.28	159.20	172.92
	13	268.75	134.73	172.92
	18	296.22	107.26	172.92

2.1.2. Solvent synthesis

All the chemicals for the solvent method remained unchanged, except for adding 10 mL of acetonitrile (ACN; Sigma-Aldrich). Additionally, the weights used for the preparation, are highlighted in table 2.1, correspond to 10 wt% LPSC for an EO: Li^+ ratio of 13:1 and 18:1. The solvent approach begins by first homogeneously grinding the dry powders of PEO, LiTFSI, and LPSC, and then transferring them to a glass vial. The addition of 10 mL ACN follows this. Next, the mixture is stirred with a magnetic stirrer for 24 hours. Subsequently, the slurry is cast onto a teflon plate and left to dry for 24 hours in a glovebox. This step allows the membrane to be set before it is placed in an antechamber with reduced pressure for 72 hours to remove any residual solvent.

2.2. Materials characterisations

2.2.1. Differential scanning calorimetry

Differential Scanning Calorimetry (DSC) is a widely used thermal analysis technique for determining materials' key thermal and physical properties. The principle of this technique involves scanning a sample in a crucible and measuring the sample's heat flow rate (Φ) versus a reference crucible as a function of time and temperature [49]. There are two main types of DSC calorimeters, power-compensated DSC and heat flux DSC . However, this report will focus on heat flux DSC due to the equipment being used for experimentation. In heat flux DSC, both the sample and the reference are subjected to the same heat source. During the temperature scan, a phase transition within the sample may occur. When this happens, the system does not maintain a steady-state equilibrium. Instead, this transition generates a signal. This signal arises because of the differences in heat flow rates between the sample and the reference [49]. These differences are further represented by equation 2.1.

$$\Phi = \frac{T_S - T_R}{R_{th}} \tag{2.1}$$

where T_S and T_R are the temperatures of the sample and reference, respectively, and R_{th} represents the thermal resistance of the sensor.

The resulting data is plotted with the vertical axis measuring the heat flow rate and the x-axis representing temperature. Important thermodynamic properties, such as the T_g, crystallisation temperature T_C, and T_m, are further visualised by figure 2.2 [50]. Furthermore, the enthalpy changes ΔH of these thermal transitions, specifically T_m and T_C, can be calculated as the area under the curve of the peaks through equation 2.2.

$$\Delta H = \int_{T_{\text{start}}}^{T_{\text{end}}} \Phi \, dt \tag{2.2}$$

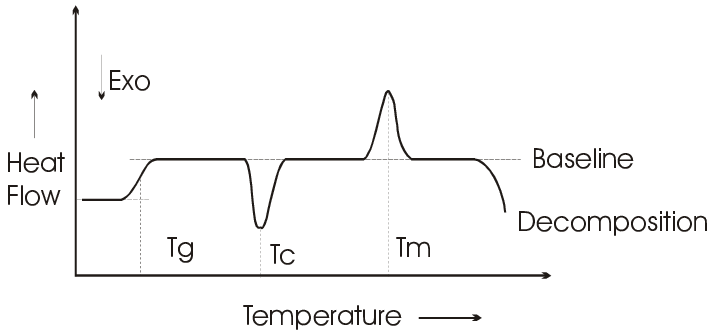

Figure 2.2: DSC curve, endothermic up, highlighting T_g, crystallisation temperature T_C, and melting transition temperature T_m of a polymer [50].

Experimental
DSC scans were performed to assess the thermal properties of HSE, utilising a TA Q2000 DSC calorimeter. The samples were initially finely cut into pieces, weighing approximately 8-14 mg, and sealed in aluminium Tzero Hermetic Pans. Next, the samples were placed in the calorimeter and scanned from -80°C to 80°C at a heating rate of 10 °C/min, with measurements taken against an empty Tzero reference pan. Subsequent analysis was performed using TA Instruments Universal Analysis 2000 software. Finally, the degree of crystallinity for the HSE was calculated using equation 2.3.

$$\chi_c = \frac{\Delta H}{\Delta H_c} \times 100 \tag{2.3}$$

Here, ΔH represents the melting enthalpy from the DSC scan, and ΔH_c corresponds to the melting enthalpy of pure PEO 600,000 g/mol.

2.2.2. X-ray photoelectron spectroscopy

X-ray Photoelectron Spectroscopy (XPS) is a powerful, non-destructive technique utilised for the surface analysis of materials. It involves projecting X-rays, typically around 6 keV, onto a material's surface in a vacuum and measuring the kinetic energy of the electrons emitted [51]. The photoelectric effect equation 2.4 can explain this phenomenon:

$$E_{\text{kin}} = h\nu - \Phi - E_{\text{BE}} \tag{2.4}$$

Here, $h\nu$ represents the energy of the X-ray photons, E_{BE} is the binding energy of the electrons in the concerned orbital, E_{kin} is the kinetic energy of the ejected photoelectrons, and Φ denotes the work function of the material. A restriction of this technique, however, is that the low energy of the X-rays used means the depth they can examine is quite shallow, usually only up to 10 nanometres [51].

Experimental
XPS analysis was performed externally at IPREM UMR CNRS 5254. This was achieved using Thermo Scientific Escalab 250Xi equipped with Al Kα radiation at 1450 eV, and subsequent data analysis was performed using the Casa XPS software.

2.3. Electrochemical characterisation

2.3.1. Electrical impedance spectroscopy

Electrochemical Impedance Spectroscopy (EIS) is a powerful, non-destructive technique used to measure the conductivity of solid-state electrolytes. EIS experiments commonly involve applying a small sinusoidal voltage perturbation, i.e., 10 mV, across a wide frequency range from very high (10 MHz) to very low (0.1 Hz) [52]. Subsequently, the system responds to the voltage by allowing AC to flow through it, allowing impedance to be determined. However, unlike resistance described by Ohm's Law, impedance is a complex value, as seen by the equation 2.5 below, which includes resistive R and reactance components X.

$$Z = R + jX \tag{2.5}$$

Analysis of EIS spectra are typically visualised through Nyquist and Bode plots illustrated in figure 2.3 a) and b), respectively. In the Nyquist plot, the imaginary impedance component is plotted on the

vertical axis against the real component on the horizontal axis, capturing the behaviour at each excitation frequency. Meanwhile, the Bode plot is divided into two graphs: one reveals the magnitude of impedance as a function of frequency, and the other details the phase angle's variation with frequency. Together, Nyquist and Bode plots offer a comprehensive analysis, each complementing the other to understand better the electrochemical system being analysed. One of the major benefits of EIS is the ability to model the experimental data with an equivalent circuit using software like RelaxIS, which helps identify specific circuit elements and their values corresponding to the electrochemical properties of the system [53]. However, multiple equivalent circuits can fit the same data set, emphasising the need for a deep understanding of the system for accurate model selection.

Ionic conductivity measurements typically use a setup with two ion-blocking electrodes (often stainless steel (SS)) to prevent ion diffusion at the electrolyte-electrode interface. Parameters are then determined from an equivalent circuit model. For example, using $R_0(C_1R_1)$, where R_0 represents series resistance, R_1 represents the bulk resistance of the electrolyte, and C_1 represents bulk capacitance, as depicted in the figure 2.3 [54]. Furthermore, the ionic conductivity (σ) can be calculated using the equation 2.6, where l and A are the thickness and the area of the electrolyte and the electrode, respectively.

$$\sigma = \frac{l}{R_{\text{bulk}} \cdot A} \tag{2.6}$$

The circuit may be modified to represent these contributions with additional circuit elements depending on other resistivity influences, including interphase or grain boundary resistance. Furthermore, constant phase elements (CPE) often replace capacitors since ideal capacitive behaviour is seldom observed in electrochemical cells [52].

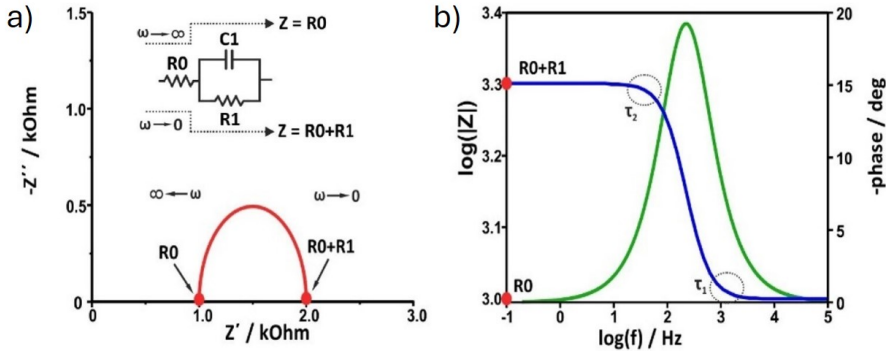

Figure 2.3: Example of Nyquist plot with $R_0(C_1R_1)$, equivalent circuit and, Bode magnitude, and phase angle plots b)[54].

Experimental

To determine the ionic conductivity of the synthesised HSE, the samples were first punched to a diameter of 16 mm and then assembled into a coin cell by placing the HSE between two 15.8 mm SS discs, which served as blocking electrodes, as depicted in figure 2.4. After securing the coin cells within a clamp, EIS measurements were performed using a Metrohm Autolab PGSTAT302N, equipped with an ECI10M high-frequency module. Additionally, the AC frequency range for the measurements using the Novo software was set from 10 MHz to 0.1 Hz. These measurements took place in an oven under varying temperature conditions. Temperatures were incrementally increased by 10°C, starting from 25°C and rising to 85°C, with each temperature maintained for 45 minutes to ensure that the coin cell reached equilibrium. Subsequently, the data was analysed, with equivalent circuit fittings of the Nyquist plots conducted using Relaxis [53]. Additionally, Arrhenius plots were generated, and relevant parameters were determined through Origin Pro.

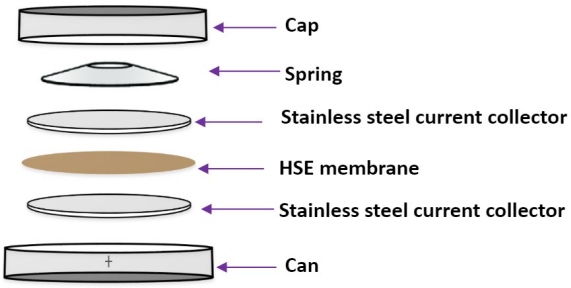

Figure 2.4: Schematic representation of coin cell setup, own work

2.3.2. Linear sweep voltammetry

Linear sweep voltammetry is a widely utilised method for analysing the stability of electrolytes. This technique involves an asymmetric cell setup comprising of a working electrode and a counter electrode. It measures the resulting current at the working electrode over time by applying a potential that linearly sweeps across both electrodes. The scan rate typically ranges from 0.01 mV/s to 10 mV/s. To assess the upper oxidation limit, an anodic sweep is performed from the operating circuit voltage (OCV) to a higher positive voltage, for example, 5 V, is performed. In contrast, the low reduction limit, a cathodic sweep is employed, by scanning from the OCV to a lower potential, i.e., $0\,\mathrm{V}$ [55]. Analysing the resulting voltammogram facilitates the determination of the lower and upper voltage limits, at the onset point of a significant current response, which signifies the electrolyte's breakdown. Furthermore, these limits can also be identified by locating the intersection point between a tangent at the maximum current and the baseline current. Alternatively, specific cut-off current densities, such as 10 µA/cm^2 and 1.0 A/cm^2, are also used to determine the breakdown limits [55].

Experimental

For the LSV experiments, an asymmetric configuration consisting of Li/HSE/SS was utilised. The setup involved placing the HSE between the reference electrode (Li metal 14 mm disc) and a SS (15.8 mm disc) as the working electrode and sealing it in a coin cell. The experiments were conducted to determine the ESW of the HSE by performing an anodic sweep from OCV to 6 V, and a cathodic sweep from OCV to 0 V, at a sweep rate of 0.1 mV/S.

3

Results and Discussion

The following chapter presents the results and discussion of two investigations. First, Section 3.1 reveals the refinements made to optimise the method of processing HSE using the dry method. Following this, Section 3.2 offers a comparative analysis of the results obtained from both the dry and solvent methods. Lastly, Section 3.3 highlights the results from a study on the influence of LiTFSI and LPSC ratios on HSE, using the dry method.

3.1. Dry method optimisation

As indicated, significant challenges arise with the dry method due to sample inhomogeneity, necessitating refinement of the process as needed. The initial preparation strategy for the HSE using the dry method involved mixing PEO and lithium LiTFSI, followed by the addition of LPSC. It was observed that PEO and LiTFSI began to coordinate and interact early on, forming a dough agglomerate, as illustrated by figure A.1. This agglomeration impeded manual grinding and the uniform integration of LPSC, presenting substantial obstacles to achieving a homogeneous mixture. Consequently, the process was modified to first mix LPSC and LiTFSI together. This modification allowed for a delayed onset of the dough formation, providing an extended period for additional mixing. As a result, despite the initial difficulties, the revised process facilitated a more uniform distribution of the LPSC within the mixture.

Despite the melting transition of PEO 69.14°C, shown in figure A.3, high temperatures were avoided to prevent potential side reactions. Therefore, an ideal temperature was determined to be just above this to facilitate effective membrane pressing. However, due to the unsealed nature of the housing device, only heat flow from the hot plate to the bottom plate was feasible, leading to a selection of 110°C, and temperatures lower than this hindered the membrane binding. A pressure of 35 bar was chosen as the working pressure. However, this pressure failed to match the thickness of the spacer (150 µm), resulting in membrane thicknesses ranging from 160 to 180 µm. Increasing the pressure allowed the membranes to reach the spacer's thickness, but pressures exceeding 45 bar risked device failure due to gauge capacity limitations. Consequently, the pressure was reduced to 35 bar to maintain the mechanical integrity of the equipment.

Selecting the appropriate non-stick material for pressing also presented challenges. Initially, 0.5 mm PTFE sheeting was used to start the membrane formation. However, due to its thickness and compressibility, it could not be pressed to less than 190 µm. Consequently, other materials were explored. For instance, aluminium (Al) foil and polyethylene terephthalate (PET) films were considered. Nonetheless, the as-prepared membrane easily adhered to the Al foil and exhibited a rubbery characteristic due to potential interactions with the PET. Therefore, a thinner PTFE sheet of 0.1 mm was utilised for compression, which was deemed an optimal choice due to its stability when heated and compressed. Furthermore, considering the flexible mechanical characteristics of the HSE, coin cells were chosen to characterise its properties, ensuring consistent pressure throughout testing.

3.2. Comparative study of the solvent and dry method

3.2.1. HSE synthesis

Four HSE membranes were prepared: two $PEO_{13}LPSC_{10}$ and two $PEO_{18}LPSC_{10}$, each using both solvent and dry methods as described in the methodology section. All samples underwent EIS, DSC, LSV tests; only the $PEO_{18}LPSC_{10}$-dry and $PEO_{18}LPSC_{10}$-solvent, were further characterised by XPS. Additionally, the $PEO_{18}LPSC_{10}$-solvent HSE for XPS, was synthesised with THF instead of ACN, yet the

preparation process remained the same.

Focusing on figure 3.1, visually comparing the membranes from each method showed only slight coloration differences. Both $PEO_{18}LPSC_{10}$ membranes displayed similar mechanical characteristics after processing and after an extended period of time. However, $PEO_{13}LPSC_{10}$ via solvent method was more flexible, adhering upon folding. In contrast, the dry method $PEO_{13}LPSC_{10}$ was initially flexible but became rigid over time.

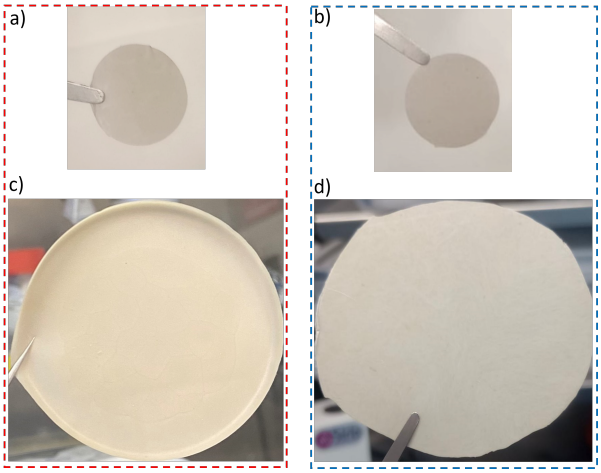

Figure 3.1: Visual comparison of HSE synthesised: a) $PEO_{13}LPSC_{10}$-solvent, shaped for coin cell testing; b) $PEO_{13}LPSC_{10}$-dry, shaped for coin cell testing; c) $PEO_{13}LPSC_{18}$-solvent as an as-cast membrane; d) $PEO_{13}LPSC_{18}$-dry method as an as-cast membrane.

3.2.2. Ionic conductivity

The Nyquist plots, obtained from EIS data at room temperature for $PEO_{13}LPSC_{10}$ and $PEO_{18}LPSC_{10}$ using both solvent and dry methods, are illustrated in figure 3.2. All Nyquist plots from variable temperature measurements were analysed using one of two equivalent circuit models proposed. The first model was used at temperatures below 55°C to represent conditions before the polymer matrix melted, and is represented by the following circuit: $L-(R_{\text{SPE}})(CPE_{\text{SPE}})-(R_{\text{ISE}})(CPE_{\text{ISE}})-CPE_{\text{Int}}$. Here L represents inductance R_{SPE} and R_{ISE} signify the resistances from the PEO-LiTFSI bulk and the LPSC bulk, respectively. The terms CPE_{SPE}, CPE_{ISE}, and CPE_{Int} represent the constant phase elements corresponding to the capacitances from the bulk PEO-LiTFSI and LPSC bulk, with CPE_{Int} denoting the capacitance of the blocking electrodes at low frequencies. Furthermore, the ionic conductivity R_{bulk} was calculated using the total of R_{SPE} and R_{ISE}, using equation 2.6. Additionally, upon increasing the temperature above the T_m of the polymer matrix, the second equivalent circuit model was applied $L-(R_{\text{ISE}})(CPE_{\text{ISE}})-CPE_{\text{Int}}$. This adjustment accounts for the absence of the bulk PEO-LiTFSI impedance and in this case, R_{ISE}, is R_{bulk}.

Arrhenius plots of the ionic conductivities at the measured temperatures range are illustrated in figure 3.3. In these plots, two linear fits were used due to the observed deflection after the melting temperatures of the polymer matrix. The observed deflection could be attributed to either the melting of the crystalline phase or the rearrangement of *-EO-* moieties [56]. Subsequently, conductivities calculated for $PEO_{13}LPSC_{10}$ at 30°C, with respect to the linear fits using the solvent and dry methods, are 1.51×10^{-5} S/cm and 1.61×10^{-5} S/cm, respectively. For, $PEO_{18}LPSC_{10}$, the ionic conductivities were found to be 8.37×10^{-6} S/cm for the solvent method and 7.61×10^{-6} S/cm for the dry method at the same temperature.

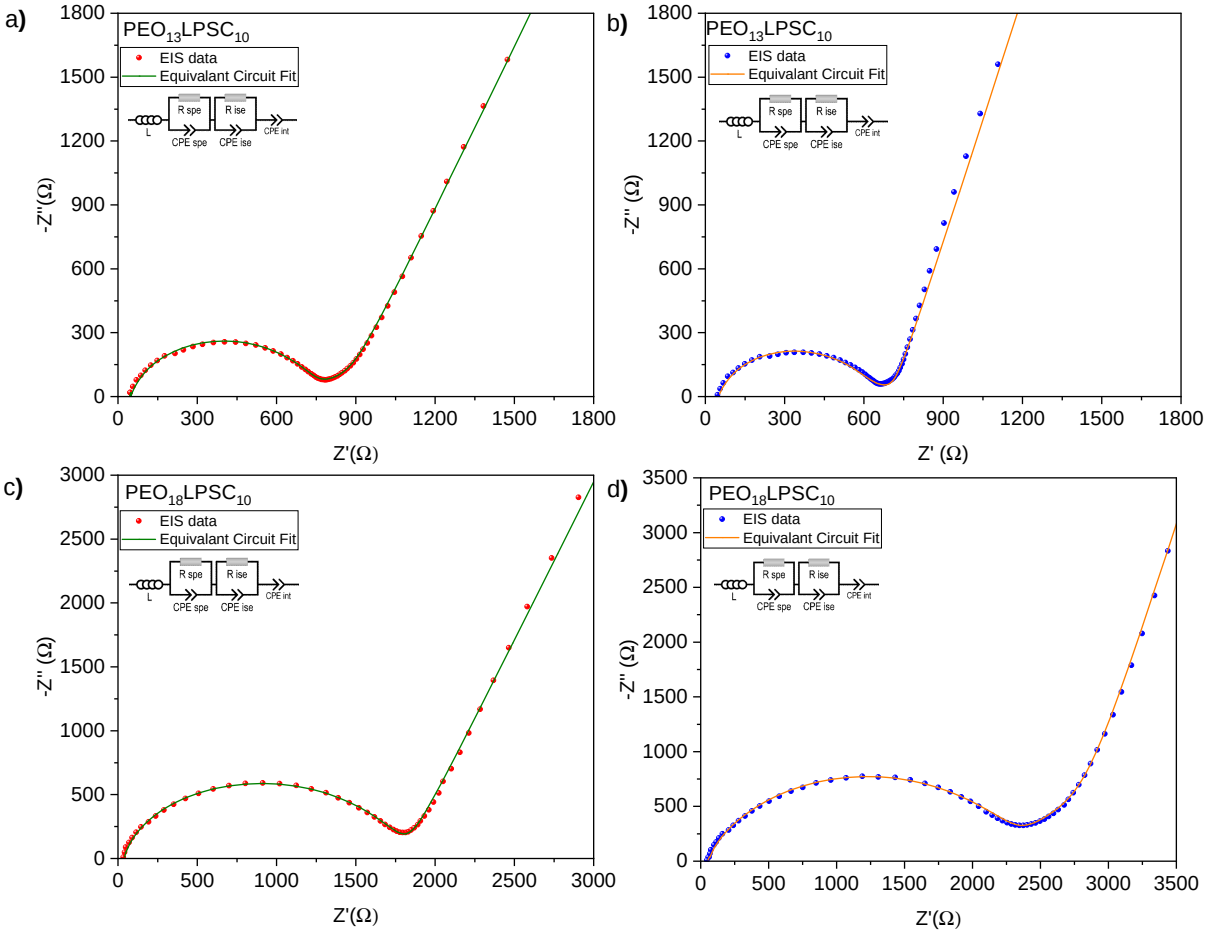

Figure 3.2: Comparison of Nyquist plots at RT (a) $PEO_{13}LPSC_{10}$-solvent HSE with a thickness of ≈150 µm, and (b) $PEO_{13}LPSC_{10}$-dry HSE with a thickness of ≈169 µm c) $PEO_{13}LPSC_{10}$-solvent HSE with a thickness of ≈150 µm d) $PEO_{13}LPSC_{10}$-dry HSE with a thickness of ≈161 µm. All samples were assembled into coin cells with the configuration SS/HSE/SS.

All HSE demonstrate high activation energies and low conductivities in the lower temperature below 55°C, a phenomenon largely due to the high crystalline regions within the SPE matrix. These regions restrict the segmental motion of the PEO chains and, consequently, impede lithium ion transport. Specifically, the activation energies for both $PEO_{18}LPSC_{10}$ HSE are notably high, calculated at 1.49 eV and 1.50 eV for the solvent and dry method, respectively, indicating the substantial energetic barriers at lower temperatures below. Conversely, at temperatures above the T_m, a notable increase in conductivities and a decrease in activation energies are observed, with values dropping below 0.5 eV for all HSE. This shift is primarily attributed to the amorphous nature of the SPE matrix at temperatures above the T_m, which facilitates a more favourable environment for lithium ion diffusion, due to enhanced free volume and segmental motion of the polymer chains. Interestingly, when comparing these activation energies an ionic conductivities with those of pure LPSC, as highlighted in figure A.2 , which exhibits an activation energy of 0.24 eV and a calculated ionic conductivity at of 1.81×10^{-3} S/cm at 30°C , no enhancement in ionic conductivity is observed . In principle, the addition of LPSC should increase the conductivity of the HSE, but it may not be detectable due to the limited frequency range of EIS. Using solid-state Nuclear Magnetic Resonance (NMR) spectroscopy may reveal insights through the selective detection of nuclei, which falls within the scope of future study.

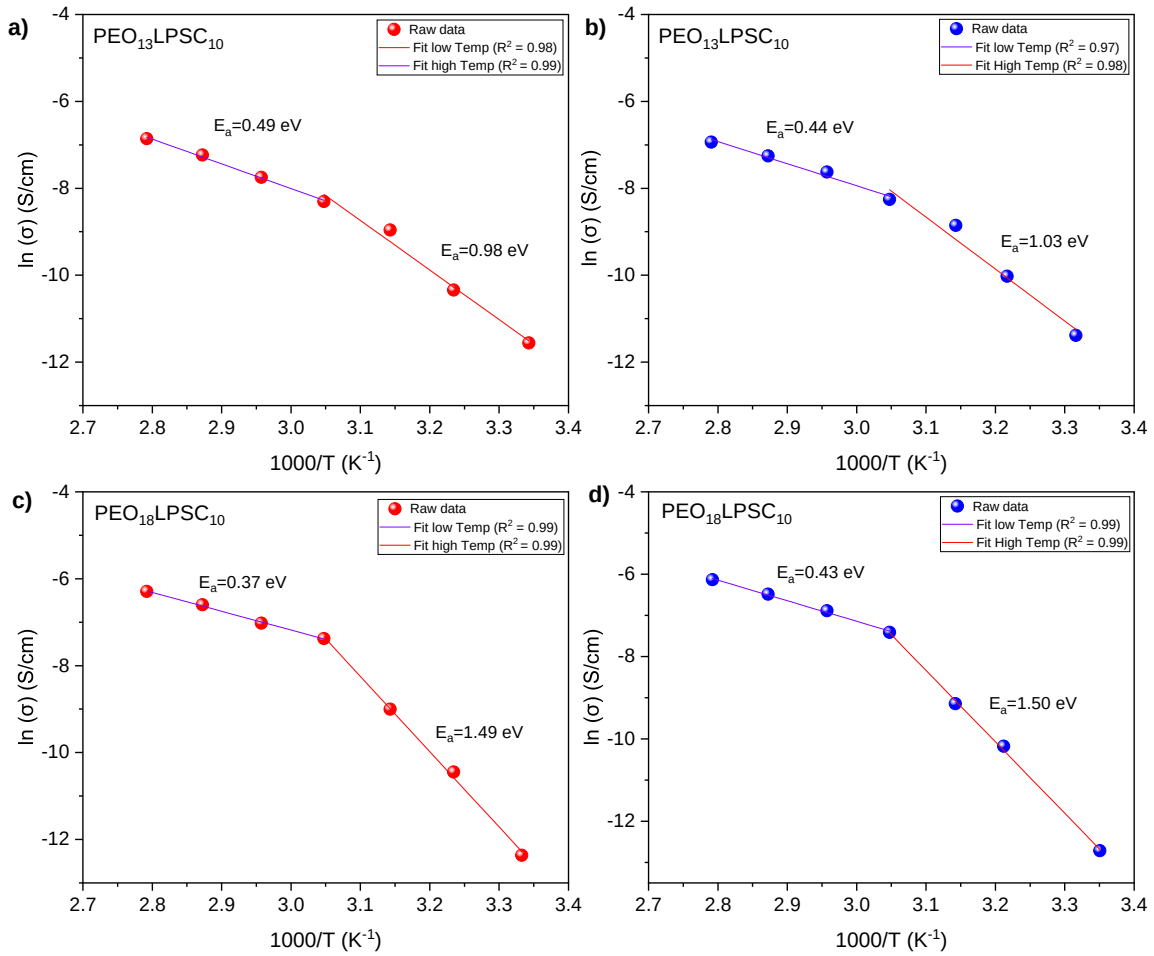

Figure 3.3: Comparison of Arrhenius plots (a) $PEO_{13}LPSC_{10}$-solvent HSE with a thickness of ≈150 µm, and (b) $PEO_{13}LPSC_{10}$-dry HSE with a thickness of ≈169 µm c) $PEO_{13}LPSC_{10}$-solvent HSE with a thickness of ≈150 µm d) $PEO_{13}LPSC_{10}$-dry HSE with a thickness of ≈161 µm. All samples were assembled into coin cells with the configuration SS/HSE/SS and measured from 25-85°C.

3.2.3. Thermal analysis

The thermal behaviour of HSE $PEO_{13}LPSC_{10}$ and $PEO_{18}LPSC_{10}$, synthesised using dry and solvent methods, was characterised through DSC and is illustrated in figure 3.4 with results summarised in table 3.1. The heat flow was normalised for comparative purposes to facilitate a clearer visual representation of the peaks.

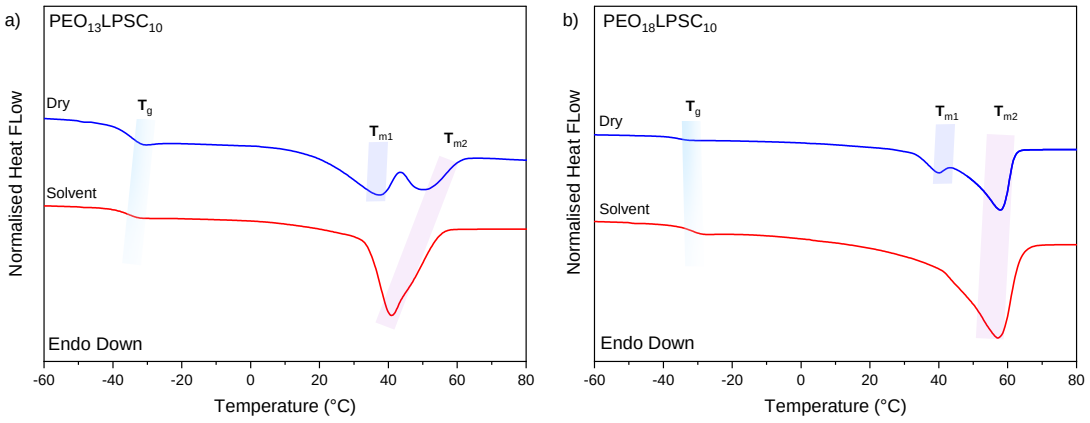

Figure 3.4: DSC scan comparing solvent and dry methods for $PEO_{13}LPSC_{10}$ and $PEO_{18}LPSC_{10}$ HSE.

In the dry synthesis approach, the DSC traces for the $PEO_{13}LPSC_{10}$-dry HSE has a T_g of 34.39°C, followed by two melting transitions at T_{m1} (36.80°C) and T_{m2} (50.84°C), with a calculated degree of crystallinity 13.02%. Comparatively for $PEO_{18}LPSC_{10}$-dry ,the T_g was slightly lower at (-34.69°C), with melting transitions at T_{m1} (39.80°C) and T_{m2} (57.77°C), and an increase in crystallinity by 15.34%. These results suggest the existence of different crystalline structures within the PEO-LiTFSI system, with T_{m1} corresponding to eutectic mixtures of PEO-LiTFSI and T_{m2} to a more stable intermediate crystalline form [16] [40]. Typically, an increase in salt concentration leads to a higher T_g and a larger amorphous region, given by the solvation of the salt in the PEO crystallites [44]. It is evident that $PEO_{13}LPSC_{10}$ exhibits a greater amorphous region compared to $PEO_{18}LPSC_{10}$. This observation is supported by the T_g trend, with $PEO_{18}LPSC_{10}$ showing a T_g that is 0.3°C lower than $PEO_{13}LPSC_{10}$.

On the other hand, DSC traces for $PEO_{13}LPSC_{10}$the DSC traces obtained from the solvent-based method revealed a T_g of -36.4°C and a single melting transition at T_{m2} of 40.90°C, with a crystallinity of 21.89%. This represents a significant increase in crystallinity compared to the dry method for the same ratio, which recorded a crystallinity of 13.02%. Furthermore, for PEO_{18}LPSC10-solvent, a T_g was observed at -31.65°C with a melting transition at T_{m2} of 57.21°C and a crystallinity of 30.55%. The absence of a lower melting transition T_{m1} in the solvent method suggests that this method may promote better dissociation of lithium salts, potentially leading to a more uniform and thermodynamically stable crystalline structure. Similarly to the dry method, the solvent method results indicate that an increase in salt concentration leads to a more amorphous phase. However, an unusual shift in the T_g was observed, where the T_g was lower for $PEO_{13}LPSC_{10}$ compared to PEO_{18}LPSC10, this is discussed more in subsequent section 3.3.2.

As highlighted in section 3.2.1, the dry method fabrication resulted in membrane $PEO_{13}LPSC_{10}$ with reduced flexibility, which progressively became more rigid over time. In contrast, $PEO_{13}LPSC_{10}$ via the solvent method maintained their initial, as-cast flexibility. The most likely explanation for the increased rigidity observed in membranes produced by the dry method is the slow crystallisation kinetics of the SPE system. The fabrication process for the dry method involves heating the polymer to temperatures above its T_m. As a result, the polymer matrix may still be in a crystallising phase post-fabrication, leading to an incomplete or delayed crystalline structure. This ongoing crystallisation can contribute to the increased rigidity observed, as the slower kinetics allow for more ordered crystalline regions to form within the SPE, enhancing its mechanical strength. This ongoing crystallisation process is supported by observations noted in figure 3.5, which show that during a second scan T_{m1} is absent. There is a decrease of the T_g by 3.8°C and a further reduction in crystallisation by 2.37%, indicating a significant change in the crystalline structure of the HSE and a slow re-crystallisation process.

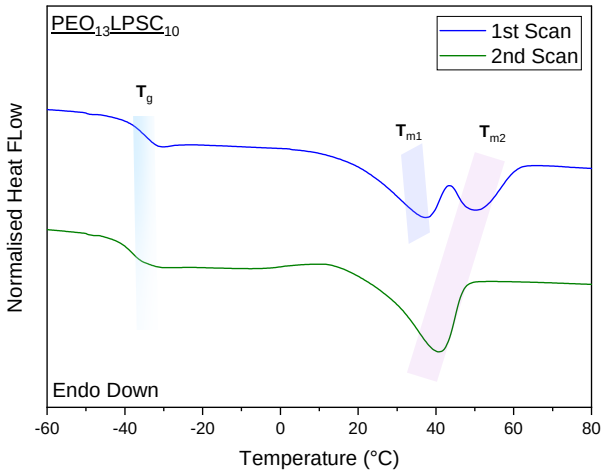

Figure 3.5: DSC scans of $PEO_{13}LPSC_{10}$-dry.

Table 3.1: Thermal behaviour for PEO with different EO:Li^+ ratios for the dry and solvent method HSE.

Scan	Method	Molar Ratio (EO:Li^+)	Tg (°C)	Tm_1 (°C)	Tm_2 (°C)	$\triangle$Hm (J/g_{PEO})	Crystallinity (%)
1	Dry	13:1	-34.39	36.81	50.84	22.14	13.02
2	Dry	13:1	-38.19	N/A	40.48	18.11	10.65
1	Solvent	13:1	-36.40	N/A	40.90	37.22	21.89
1	Dry	18:1	-34.69	39.80	57.77	58.81	36.93
1	Solvent	18:1	-31.65	N/A	57.21	51.93	30.55

3.2.4. Electrochemical stability

LSV was utilised to measure the ESW for the HSE, $PEO_{13}LPSC_{10}$ and $PEO_{18}LPSC_{10}$, for both the solvent and dry method and is illustrated in figure 3.6 and summarised in table 3.2. Further analysis were performed to determine relevant cathodic and anodic limits by analysing the exponential increase of current, using the tangent function in Origin Pro.

From figure 3.6, we can see that on the anodic sweep, the oxidation potential occurs at 3.34 V, where the full breakdown of the PEO-LiTFSI system occurs. On the other hand, a cathodic sweep reveals a reduction potential and full electrolyte decomposition at 1.78 V. This can be attributed to phosphorous reduction ($P^{5+} \rightarrow P^0 - 5e^-$) with the formation of Li_2S [31]. Subsequent analyses, represented in subplots (b), (c), and (d), show an initial increase in current at approximately 2.3 V corresponding to the first oxidation potential. However, this increase in current remains below the critical current density threshold of 10 μA/cm^2, as defined by [55], suggesting that this does not represent a significant decomposition of these HSE. This occurrence is likely due to surface oxidation of LPSC, where sulphur redox is active ($S^{2-} \rightarrow S^0 + 2e^-$), leading to the formation of P_2S_5 and because a relatively small composition of 10 wt% of LPSC in combination with PEO-LiTFSI no major oxidation occurs. Furthermore, there is a stabilisation period from 3 V, followed by a second oxidation potential and the full breakdown of the HSE occurring at 4.81 V, 4.49 V, and 4.67 V for $PEO_{13}LPSC_{10}$-dry, $PEO_{18}LPSC_{10}$-solvent, and $PEO_{18}LPSC_{10}$-dry respectively. In the cathodic sweep, no passivation occurs, and the reduction potential corresponds to the full breakdown of the electrolyte for $PEO_{13}LPSC_{10}$-dry, $PEO_{18}LPSC_{10}$-solvent, and $PEO_{18}LPSC_{10}$-dry occurs at 1.78 V, 1.59 V, and 1.79 V, respectively.

Overall, the results demonstrate that the introduction of the organic phase has significantly widened the ESW of LPSC from 1.25 V to 1.73 V, 3.03 V, 2.70 V and 2.95 V for $PEO_{13}LPSC_{10}$ -solvent, $PEO_{13}LPSC_{10}$-dry, $PEO_{18}LPSC_{10}$-solvent and $PEO_{18}LPSC_{10}$-dry respectively [30]. Moreover, the dry method shows enhanced stability compared to the solvent method, suggesting its potential to improve electrolyte performance.

Table 3.2: LSV summary of different EO:Li^+ ratios for the dry and solvent method HSE.

Processing method	HSE	Lower limit (V)	Upper limit (V)	Potential Window on SS (V)
Solvent	PEO13LPSC10	1.61	3.34	1.73
Dry	PEO13LPSC10	1.78	4.81	3.03
Solvent	PEO18LPSC10	1.79	4.49	2.70
Dry	PEO18LPSC10	1.72	4.67	2.95

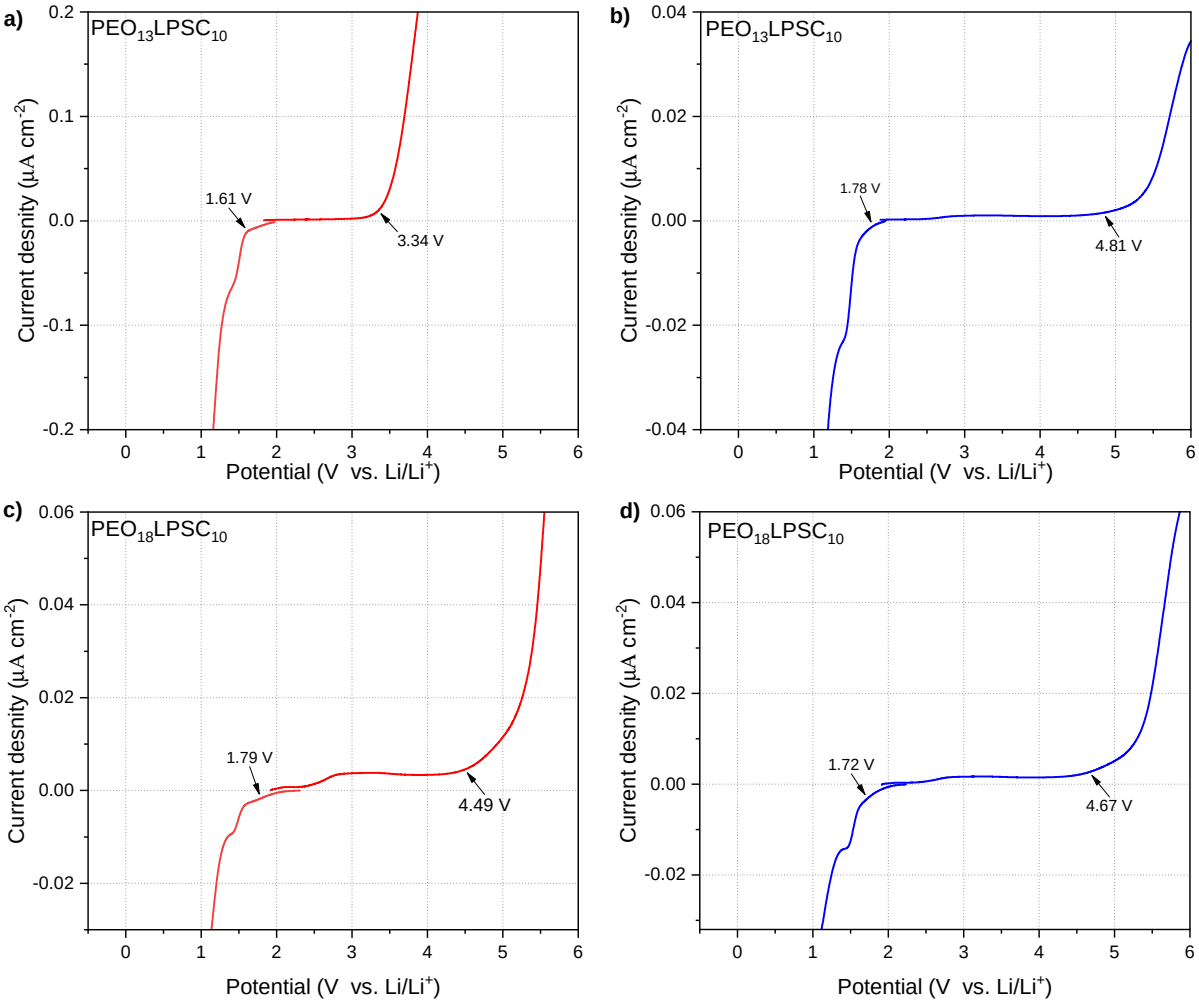

Figure 3.6: Comparison of LSV curves: (a) $PEO_{13}LPSC_{10}$-solvent HSE with a thickness of ≈150 µm, and (b) $PEO_{13}LPSC_{10}$-dry HSE with a thickness of ≈169 µm c) $PEO_{18}LPSC_{10}$-solvent HSE with a thickness of ≈150 µm d) $PEO_{18}LPSC_{10}$-dry HSE with a thickness of ≈161 µm. All samples were assembled into coin cells with the configuration Li/HSE/SS.

3.2.5. XPS

XPS analysis of the top and bottom surfaces of dry and solvent pristine $PEO_{18}LPSC_{10}$ samples was conducted. Subsequently, high-resolution spectra for C 1s and S 2p, labelled as a) and b) respectively, are illustrated in figure 3.7 and summarised in table 3.3. In figure 3.7, part a), the C 1s spectrum is divided into five contributions. Two of these peaks result from the original, unreacted PEO and LiTFSI, while the other two are indicative of PEO decomposition products. Additionally, a peak results from hydrocarbon contamination, which is unavoidable due to the influence of the atmosphere in which these samples were processed. The corresponding peaks for the unreacted PEO and LiTFSI occur at 286.5 eV $(OCH_2-CH_2-)_n$ and 292 eV ($-CF_3$), respectively. The decomposition products of PEO are represented by peaks for CO_3 and $-COOR$ at 288 eV and 295.5 eV, respectively. Furthermore, the peak at 285 eV ($-CH_2-$) is related to hydrocarbon contamination [16]. Moreover, in Figure 3.7 part b), four contributions to S 2p have been deconvoluted into four distinct doublet peaks, two of which are attributed to unreacted LiTFSI (TFSI) at 171 eV and LPSC (-P-S-Li) at 161.7 eV [16]. Furthermore, the decomposition products are identified, with $-SO_2CF_3$ assigned at 168 eV and oxidised LPSC ($-S_x$) at 163 eV [16]. Additionally, based on these assigned species for both C 1s and S 2p, the origin of these species was evaluated and further categorised into surface contamination, PEO, LiTFSI, and LPSC, as detailed in table 3.4.

Comparing the contributions of each species for the dry method at both the top and bottom, we observe a very similar contribution of each species occurring in both regions, except for hydrocarbon contamination, which is more evident at the bottom. Similarly, in the solvent method, C1 s hydrocarbon contamination is evident in the top and bottom, with other COOR appearing almost exclusively on the

bottom surface. However, comparing the two methods, it is clear that hydrocarbon contamination is more present in the solvent method, whereas $(OCH_2-CH_2-)_n$ and COOR species are more evident in the dry method. Shifting focus to the S 2p in figure 3.7 part b), we see very similar contributions of all four assigned species in both regions for the dry membrane top and bottom. Meanwhile, for the solvent method, the top and bottom show slight variances in contributions, with the solvent top compared to the bottom. When comparing the two methods $-SO_2CF_3$ and $-S_x$ and –P–S–Li species are more present in the solvent method.

Although XPS is a surface analysis, both membranes appear to show homogeneity when comparing both surfaces. Furthermore, the solvent method reveals a more significant portion of decomposition overall for $-SO_2CF_3$ and $-S_x$. Despite the low polarity of the THF solvent used, when comparing the decomposition products of the $-SO_2CF_3$ and $-S_x$, we can see that the solvent has had a more significant impact on the decomposition of the samples using this processing method over the dry method.

Table 3.3: Binding energy of assigned species corresponding to C1 S and S 2p spectra.

Spectrum	Assigned Species	Binding energy (eV)
C 1s	$-CH_2-$	285
	$(OCH_2-CH_2-)_n$	286.5
	$-COOR$	288
	CO_3	289.5
	$-CF_3$	292
S 2p	TFSI	171
	$-SO_2CF_3$	168
	$-S_x$	163
	$-P-S-Li$	161.7

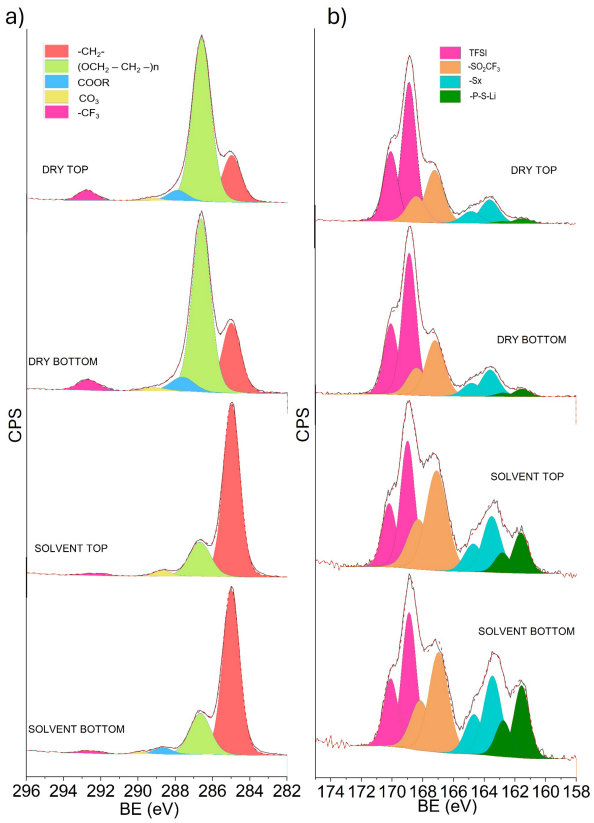

Figure 3.7: XPS surface analysis: a) C 1s spectra, b) S 2p spectra for $PEO_{18}LPSC_{10}$ using solvent and dry synthesis.

Table 3.4: Species Allocation of HSE surface measurements.

Processing Method	Species Allocation	HSE Top Surface (%)	HSE Bottom Surface (%)
Dry	Surface contamination	11.37	15.1
	PEO	51.85	48.37
	LiTFSI	25.22	25.27
	LPSC	0.84	1.27
	total	91.59	92.32
Solvent	Surface contamination	64.43	63.83
	PEO	15.07	16.41
	LiTFSI	10.45	7.875
	LPSC	1.67	2.15
	total	93.374	91.41

3.2.6. Conclusion of comparative analysis

The results highlight that two processing methodologies for HSE provide comparable outcomes, specifically in terms of ionic conductivity. EIS results show that the ionic conductivity for the dry-processed at 30° C $PEO_{13}LPSC_{10}$ is higher than its solvent-processed counterpart. However, for $PEO_{18}LPSC_{10}$, the dry method results in lower ionic conductivity at 30° C conductivity compared to the solvent method. Thermal analysis indicates that heating above the melting transition of the polymer results in a slow crystallisation period for the dry method, which has resulted in two crystalline phases. In contrast, the solvent method exhibits a single crystalline phase after processing.This indicates that the dry method may display different electrical performance over time. XPS analysis reveals that membranes display homogeneity when comparing the top and bottom surfaces, when comparing the two membranes from different processing methods, they exhibit different compositions on their respective surfaces. Furthermore, side reactions leading to the decomposition of the HSE occur in both the dry and solvent methods and or more significant in the dry method.

3.3. Alteration of LiTFSI and LPSC on HSE, using dry synthesis

Initial, this study aimed at exceeding a LPSC ratio of 40%, as reported by [16], which demonstrated an ionic conductivity of 5.90×10^{-5} S/cm at 30°C using the solvent method, and aimed to determine if the dry method could produce comparable results. However, this study was constrained to a maximum of 30 wt% LPSC. This limitation is demonstrated in figure 3.8, which shows that a uniform membrane could not be achieved with thicknesses varied across the membrane with sections exceeding 250 µm, even at an EO:Li^+ ratio of 10:1, which had shown the highest coordination with PEO. Subsequently, the study explored three EO:Li^+ ratios of 10:1, 13:1, and 18:1, with LPSC ratio at 10, 20, and 30 wt%. Notable observations post-HSE processing exhibited similar phenomena as described in section 3.2.1. Specifically, for low EO:Li^+ ratios (10:1 and 13:1) across the LPSC ratio range of 10–30 wt%, the HSE initially remained very flexible but gradually became more rigid over time. In contrast, all EO:Li^+ ratios of 18:1 maintained their as-processed flexibility. Moreover, an increase in the ratio of LPSC resulted in less flexible membranes across all measured EO:Li^+ ratios.

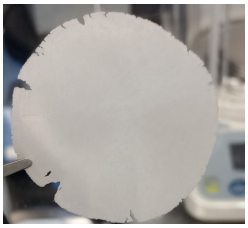

Figure 3.8: Visual of, $PEO_{10}LPSC_{40}$ processed using the dry method.

3.3.1. Ionic conductivity

Nyquist plots for all 10 wt% and 20 wt% samples and $PEO_{18}LPSC_{30}$ were fit with the two equivalent circuits described . However, the $PEO_{10}LPSC_{30}$ and $PEO_{13}LPSC_{30}$ required additional circuit elements $(R_{\text{IP}})(CPE_{\text{IP}})-$ to account for a new interface representing the interface between the bulk LPSC and the bulk PEO-LiTFSI. Subsequently, for this circuit, R_{bulk} was determined as $R_{\text{spe}} + R_{\text{se}} + R_{\text{ip}}$. Again, above the T_m, the circuit $L - (R_{\text{ISE}})(CPE_{\text{ISE}}) - CPE_{\text{Int}}$ was used as the two resistances, R_{SPE} and R_{IS}, were no longer present. Furthermore Nyquist plots of all EO:LI^+ 13:1 ratios are illustrated in figure 3.9, to highlight the influence of different resistances on the impedance. Interestingly, in $PEO_{18}LPSC_{30}$, the R_{IP} was not present, most probably due to the lower salt ratio and therefore no physical interface between the bulk LPSC and bulk PEO-LiTFSI.

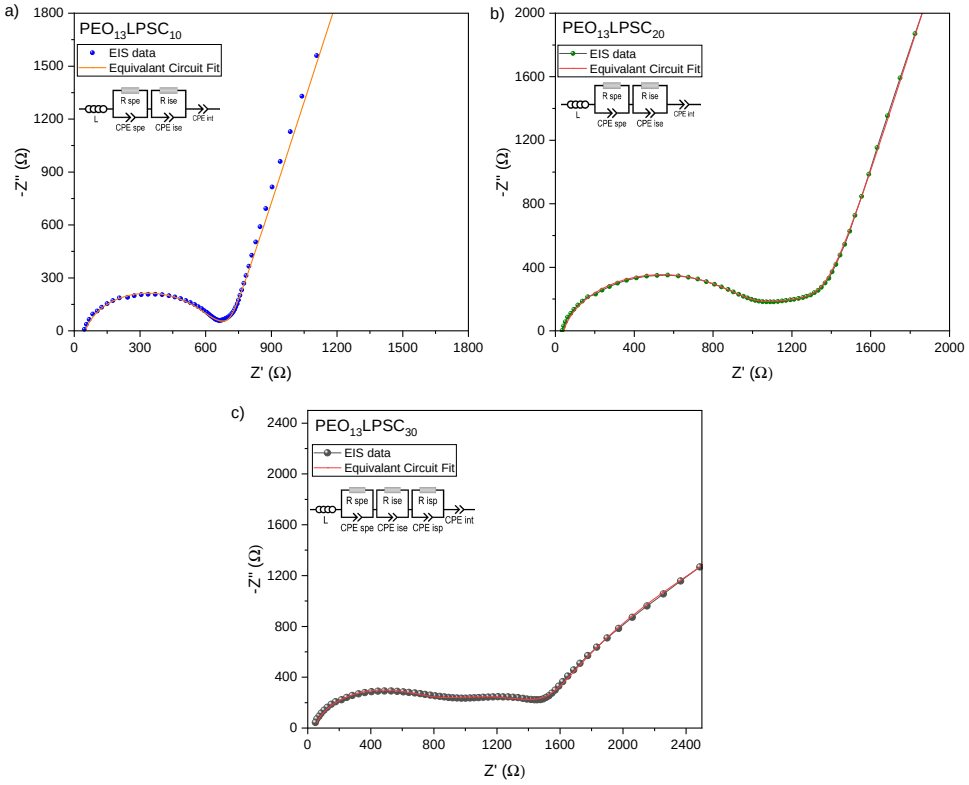

Figure 3.9: Comparison of Nyquist plots at RT: (a) $PEO_{13}LPSC_{10}$ HSE, with a thickness of ≈169 µm, and (b) $PEO_{13}LPSC_{20}$, HSE with a thickness of ≈150 µm c) $PEO_{13}LPSC_{30}$, HSE with a thickness of ≈150 µm.

Furthermore, Arrhenius plots are presented in A.4, A.5, A.6 for the 10 wt%, 20wt% and 30wt% respectively, with two linear fits applied, and results summarised in table 3.5. From the results, three ionic conductivities exceed 10^{-5} S/cm at 30°C: $PEO_{10}LPSC_{10}$, $PEO_{13}LPSC_{10}$, and $PEO_{10}LPSC_{20}$. The highest ionic conductivity is observed at the 10:1 EO:Li^+ ratio, with a value of 3.35×10^{-5} S/cm. The ratio with the lowest conductivities across all measured LPSC ratios is the 18:1 EO:Li^+, where the conductivity remains fairly stagnant from 10 to 30 wt%. Additionally, increasing the LPSC ratio from 10 to 30 wt% does not improve ionic conductivities of almost all the studied electrolytes, apart from EO:Li^+ 18:1 which only resulted in a minor increase at a 20 wt% followed by further a decrease at 30 wt%. Instead, the increase in LPSC ratio appears to lead to a more resistive and tortuous path for Li-ion diffusion, impeding the segmental motion of the polymer chains potentially because of the formation of the LPSC particle clusters.

Table 3.5: Ionic conductivities of HSE with varied LPSC content and EO:Li^+ ratios processed using the dry method.

LPSC wt%	Molar Ratio EO:LI^+	Ionic Conductivity (σ_{ion} = S/cm) 30 °C	50 °C	80 °C	Low Temp. Ea (eV)	R^2	High Temp. Ea (eV)	R^2
10	10:1	3.35×10^{-5}	2.35×10^{-4}	9.88×10^{-4}	0.82	0.97	0.45	0.99
	13:1	1.61×10^{-5}	1.84×10^{-4}	8.37×10^{-4}	1.03	0.96	0.44	0.98
	18:1	7.61×10^{-6}	2.63×10^{-4}	1.83×10^{-3}	1.50	0.99	0.43	0.99
20	10:1	1.59×10^{-5}	1.50×10^{-4}	8.51×10^{-4}	0.95	0.95	0.54	0.95
	13:1	9.80×10^{-6}	1.31×10^{-4}	9.46×10^{-4}	1.10	0.99	0.56	0.98
	18:1	7.67×10^{-6}	1.37×10^{-4}	7.30×10^{-4}	1.22	0.99	0.35	0.98
30	10:1	8.64×10^{-6}	7.25×10^{-5}	5.93×10^{-4}	0.90	0.99	0.65	0.99
	13:1	7.31×10^{-6}	5.59×10^{-5}	3.09×10^{-4}	0.86	0.99	0.44	0.98
	18:1	7.44×10^{-6}	1.29×10^{-4}	7.26×10^{-4}	1.20	0.99	0.45	0.98

3.3.2. Thermal analysis

The thermal behaviour of HSE, processed using the dry method for EO:Li^+ ratios of 10:1, 13:1, and 18:1, along with three different ratios of LPSC, 10 wt%, 20 wt%, and 30 wt% was characterised through DSC. This is illustrated in figure 3.10 and summarised in table 3.6. As indicated in table 3.6, a higher salt concentration was observed to reduce crystallinity across all analysed LPSC wt%. Furthermore, crystallinity decreased as the LPSC ratio increased for the EO:Li^+ ratios. This trend aligns with the literature, which identifies LPSC and LiTFSI's roles as plasticisers on the SPE [16][39]. Moreover, the lower the crystallinity aligns with, the higher ionic conductivity observed in 3.3.1. However, there is a contradiction here, as the ionic conductivity should be highest for the HSE with the lowest degree of crystallinity. This may be due to uneven LPSC distribution within the PEO matrix, leading to particle aggregation. As a percolation network through the LPSC phase is unlikely at these LPSC concentrations, the diffusion pathway would still be through the organic phase. The subsequent agglomeration of LPSC would therefore create a more tortuous and less efficient diffusion path for lithium ions, leading to a lower ionic conductivity.

Except for the $PEO_{18}LPSC_{30}$ sample, all HSEs analysed exhibited two melting transitions, indicating two distinct crystalline phases, as mentioned in 3.2.3. Focusing on the T_g, slight temperature variations are evident, For lower LPSC concentrations (10% and 20%), the influence of salt concentration is more evident (the higher the salt concentration, the lower the Tg). However, when the LPSC ratio is increased to 30%, the effect of salt concentration becomes less pronounced, potentially due to the accumulation of LPSC particles. Further investigations are suggested to verify this.

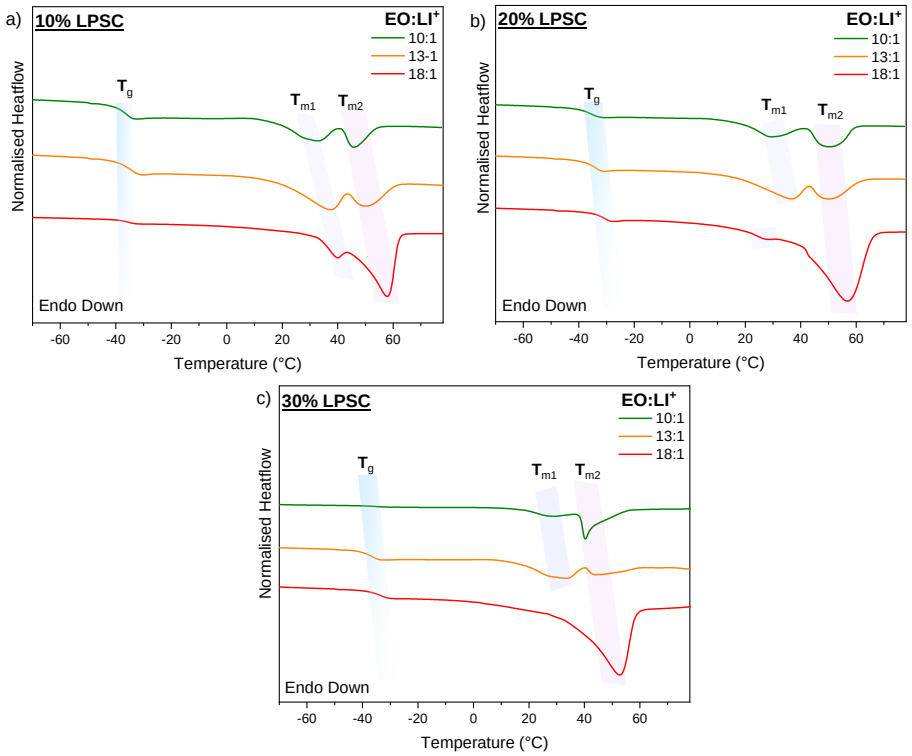

Figure 3.10: DSC scans of HSE with varied LPSC: a) 10 wt% LPSC b) 20 wt% LPSC and C) 30 wt% LPSC content at different $EO:Li^+$ ratios, processed using the dry method.

Additionally, there is a likelihood of inconsistency in the data due to the sample preparation process. Multiple small pieces of the HSE were used to fill the pan floor as if they were a single piece. Although the specific mass range suitable for the Tzero pans (901683.901) used in these experiments was not explicitly outlined in the [57], an alternative exists in the form of Tzero Low-Mass Pans (901670.901), which are designed better to accommodate smaller samples (less than 10 mg). Utilising these pans could allow for a single section of HSE rather than compressing multiple sections onto the pan floor. This method could lead to more uniform heating of the HSE, thereby enhancing the reliability and consistency of the thermal analysis results by minimising the variability introduced using multiple HSE sections.

Table 3.6: Thermal behaviour of HSE with varied LPSC content and $EO:Li^+$ ratios processed using the dry method

LPSC Content (wt%)	Molar ratio ($EO:Li^+$)	Tg (°C)	Tm_1 (°C)	Tm_2 (°C)	ΔHm (J/g_{PEO})	Crystallinity (%)
10	10:1	−36.31	31.63	45.95	22.14	13.02
	13:1	−34.39	36.81	50.84	23.71	13.95
	18:1	−34.69	39.80	57.77	62.78	36.93
20	10:1	−35.69	28.88	50.5	18.55	10.91
	13:1	−33.62	36.58	51.25	23.07	13.57
	18:1	−31.84	25.93	55.65	47.81	28.12
30	10:1	−35.25	27.35	40.57	9.81	5.57
	13:1	−36.33	32.25	44.02	10.41	6.12
	18:1	−33.67	N/A	52.75	33.67	19.63

3.3.3. Electrochemical stability

LSV was set out to determine the ESW of all electrolytes in this study. Only the anodic sweep was achievable for the full set of samples, attributed to the difficulty in cell assembly, which resulted in many of these sweeps being repeated numerous times because of significant contact loss during measurements. Due to the observed slow crystallisation period, continuous fresh samples had to be processed to accommodate for this. For these reasons, the study was limited to two samples $PEO_{10}LPSC_{10}$ and

$PEO_{10}LPSC_{30}$ to study the effect of the LPSC ratio on the two ends of the LPSC ratio range. Moreover, the results of the LSV scans are illustrated in figure 3.11 and summarised in table 3.7.

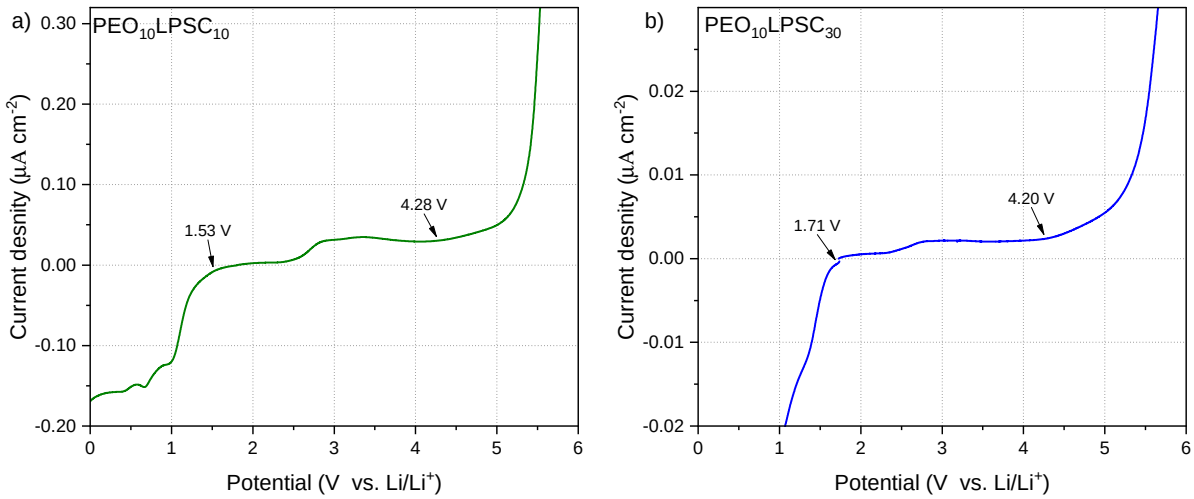

Figure 3.11: Comparison of LSV curves (a) $PEO_{10}LPSC_{10}$ solvent HSE with a thickness of ≈161 µm, and (b) $PEO_{10}LPSC_{30}$ Dry HSE with a thickness of ≈169 µm

Table 3.7: Electrochemical stability for $PEO_{10}LPSC_{10}$ and $PEO_{10}LPSC_{30}$

HSE	Lower limit (V)	Upper limit (V)	Potential stability window on SS (V)
PEO10LPSC10	1.53	4.28	2.75
PEO10LPSC30	1.71	4.20	2.49

Comparing a) and b) from figure 3.11, we see observations similar to those described in 3.2.4. For the anodic scan, an initial current rise at approximately 2.3 V and passivation at 3 V for both HSE followed by the full electrolyte degradation at 4.28 V and 4.20 V for $PEO_{10}LPSC_{10}$ and $PEO_{10}LPSC_{30}$, respectively. Interestingly, although there is a significant increase in LPSC from 10-30 wt%, a stabilisation still occurs. The reduction potential occurs much sooner at 1.71 V for $PEO_{10}LPSC_{30}$ compared to the 1.53 V for $PEO_{10}LPSC_{10}$. Moreover, the potential window on SS is greater for the $PEO_{10}LPSC_{10}$ compared to $PEO_{10}LPSC_{30}$, which is a result of the lower ratio of LPSC and consequently a higher redox activity.

3.3.4. Conclusion of LiTFSI and LPSC on HSE investigation

From this study, the EIS data indicates that an increase in a LPSC ratio in the HSE leads to a more resistive and tortuous path for Li-ion diffusion, impeding the segmental motion of the polymer chain and thus resulting in lower ionic conductivity for all but the EO:Li^+ ratio of 18:1, which showed an increase from 10 to 20 wt% LPSC, followed by a further decrease at 30 wt%. In contrast, the DSC highlights that LPSC and LiTFSI are acting as plasticisers by reducing the degree of crystallinity of PEO by disrupting the orderly arrangement of polymer chains, thereby enhancing the material's amorphous nature and the segmental motions of the polymer chains. The contradiction between EIS and DSC findings can be explained by the balance between the inorganic and organic phases in the HSE. Initially, LPSC and LiTFSI, improve the amorphous nature and mobility of the polymer. However, beyond 10 wt%, agglomeration of LPSC may occur, and therefore create a more tortuous and less efficient diffusion path for lithium ions as percolation through the LPSC phase has not yet been established. Furthermore, LSV reveals a 30 wt% LPSC ratio and EO:Li^+ ratio of 10:1, leads to a more narrow ESW, compared to 10 wt% with the same EO:Li^+ ratio, due to the earlier decomposition of the LPSC within the organic phase.

4

Conclusion and recommendations

Conclusions

This study concentrated on the PEO-LiTFSI-LPSC system. Two investigations were conducted, leading to the conclusions outlined below:

Comparative study of solvent and dry method

- Ionic conductivity of the dry-processed $PEO_{13}LPSC_{10}$ at 30°C is higher than its solvent-processed counterpart. However, for $PEO_{18}LPSC_{10}$, the dry method yields lower ionic conductivity at 30°C.
- All HSE demonstrate high activation energies and low conductivities in the lower temperature region. Conversely, above the melting point, T_m, low activation energies and high ionic conductivities are experienced due to enhanced free volume and enhanced segmental motion of the polymer chains.
- Heating above the T_m of the polymer causes a slow crystallisation for HSE using the dry method, which results in two crystalline phases. In contrast, the solvent method exhibits a single crystalline phase after processing.
- XPS analysis indicates homogeneity across the top and bottom surfaces of membranes but reveals compositional differences between membranes produced by different methods. Additionally, side reactions resulting in HSE decomposition were observed in both dry and solvent processing techniques, however less significant in the dry method.
- The dry method shows enhanced stability compared to the solvent method, suggesting its potential to improve electrolyte performance.

Alteration of LiTFSI and LPSC on HSE, using dry synthesis

- An increase in LPSC ratio from 10 wt% to 30 wt% leads to a more resistive and tortuous path for Li-ion diffusion, impeding the segmental motion of the polymer chain and thus resulting in lower ionic conductivity for all but $PEO_{18}LPSC_{20}$.
- LPSC and LiTFSI act as plasticisers by reducing the degree of crystallinity of PEO by disrupting the orderly arrangement of polymer chains, thereby enhancing the material's amorphous characteristics. However, beyond 10 wt%, agglomeration of LPSC may occur, and therefore create a more tortuous and less efficient diffusion path for lithium ions through the organic phase, leading to lower ionic conductivities.
- A 30 wt% LPSC ratio and EO:Li^+ ratio of 10:1, leads to a more narrow ESW, compared to 10 wt% with the same EO:Li^+ ratio, due to the earlier decomposition of the LPSC within the organic phase.

Recommendations

- Study the crystalline changes of the HSE after processing and for an extended period, using SEM to determine if a slow crystallisation period indeed exists from elevated temperatures above the T_m.
- Alternatively, elevate the temperature during the solvent method above the T_m of the HSE using solvent analysis and then characterise through DSC to see if an additional crystalline peak is observed.

- Utilise Tzero Low-Mass Pans (901670.901) during DSC analysis to allow for greater sensitivity at weights < 10mg.
- Perform NMR to investigate the influence of LPSC on the Li-conduction network and to determine whether its role extends beyond its plasticising effect in the HSE system.
- Increase the working pressure during hot pressing to allow for the binding of LPSC with PEO-LiTFSI above 30 wt%.
- Use stainless steel 316 sheeting over PTFE as it should not chemically interact with the HSE and avoid warping of sheeting during high compression at high LPSC ratios.
- Perform additional electrochemical characterisation techniques (cycling the cells, stability with plating and stripping tests) to determine which LPSC and EO:Li^{+} ratio results in the optimal HSE compositions. Further expand on the analysis and reach a more definitive conclusion about the better processing method.

Bibliography

[1] Stephan Leuthner. “Lithium-ion battery overview”. In: *Lithium-Ion Batteries: Basics and Applications*. Ed. by Reiner Korthauer. Berlin, Heidelberg: Springer Berlin Heidelberg, 2018, pp. 13–19. ISBN: 978-3-662-53071-9. DOI: 10.1007/978-3-662-53071-9_2.

[2] *Batteries - European Commission*. URL: https://environment.ec.europa.eu/topics/waste-and-recycling/batteries_en (visited on 03/09/2024).

[3] *Burnt-out Fremantle Highway cargo ship arrives at Rotterdam port | NL Times*. URL: https://nltimes.nl/2023/09/23/burnt-fremantle-highway-cargo-ship-arrives-rotterdam-port (visited on 03/09/2024).

[4] Bin Liu, Ji-Guang Zhang, and Wu Xu. “Advancing Lithium Metal Batteries”. *Joule* **2**.(5) (2018), pp. 833–845. ISSN: 2542-4351. DOI: 10.1016/j.joule.2018.03.008.

[5] Daxian Cao et al. “Bipolar stackings high voltage and high cell level energy density sulfide based all-solid-state batteries”. *Energy Storage Materials* **48** (2022), pp. 458–465. ISSN: 2405-8297. DOI: 10.1016/j.ensm.2022.03.012.

[6] Theodosios Famprikis et al. “Fundamentals of inorganic solid-state electrolytes for batteries”. *Nature Materials* **18**.(12) (Dec. 2019). Publisher: Nature Publishing Group, pp. 1278–1291. ISSN: 1476-4660. DOI: 10.1038/s41563-019-0431-3.

[7] João C. Barbosa et al. “Toward Sustainable Solid Polymer Electrolytes for Lithium-Ion Batteries”. *ACS Omega* **7**.(17) (May 3, 2022). Publisher: American Chemical Society, pp. 14457–14464. DOI: 10.1021/acsomega.2c01926.

[8] Ming Liu et al. “Improving Li-ion interfacial transport in hybrid solid electrolytes”. *Nature nanotechnology* **17**.(9) (2022), pp. 959–967. ISSN: 1748-3395. DOI: 10.1038/s41565-022-01162-9.

[9] Yingchun Lyu et al. “An Overview on the Advances of LiCoO2 Cathodes for Lithium-Ion Batteries”. *Advanced Energy Materials* **11**.(2) (), p. 2000982. ISSN: 1614-6840. DOI: 10.1002/aenm.202000982.

[10] Tobias Placke et al. “Lithium ion, lithium metal, and alternative rechargeable battery technologies: the odyssey for high energy density”. *Journal of Solid State Electrochemistry* **21** (2017), pp. 1939–1964. ISSN: 1433-0768. DOI: 10.1007/s10008-017-3610-7.

[11] Wahid Zaman and Kelsey B. Hatzell. “Processing and manufacturing of next generation lithium-based all solid-state batteries”. *Current Opinion in Solid State and Materials Science* **26**.(4) (Aug. 1, 2022), p. 101003. ISSN: 1359-0286. DOI: 10.1016/j.cossms.2022.101003.

[12] “Diffusion Mechanisms”. In: *Diffusion in Solids: Fundamentals, Methods, Materials, Diffusion-Controlled Processes*. Ed. by Helmut Mehrer. Springer Series in Solid-State Sciences. Berlin, Heidelberg: Springer, 2007, pp. 95–104. ISBN: 978-3-540-71488-0. DOI: 10.1007/978-3-540-71488-0_6.

[13] Dominic Bresser et al. “Decoupling segmental relaxation and ionic conductivity for lithium-ion polymer electrolytes”. *Molecular Systems Design & Engineering* **4**.(4) (2019). Publisher: Royal Society of Chemistry, pp. 779–792. DOI: 10.1039/C9ME00038K.

[14] Ronan Chometon et al. “Targeting the right metrics for an efficient solvent-free formulation of PEO: LiTFSI: Li6PS5Cl hybrid solid electrolyte”. *ACS Applied Materials & Interfaces* **15**.(50) (2023), pp. 58794–58805. ISSN: 1944-8244. DOI: 10.1021/acsami.3c11542.

[15] Jin Zheng, Mingxue Tang, and Yan-Yan Hu. “Lithium Ion Pathway within Li7La3Zr2O12-Polyethylene Oxide Composite Electrolytes”. *Angewandte Chemie International Edition* **55**.(40) (2016). _eprint: https://onlinelibrary.wiley.com/doi/pdf/10.1002/anie.201607539, pp. 12538–12542. ISSN: 1521-3773. DOI: 10.1002/anie.201607539.

[16] Fabian J Simon et al. “Interphase formation of PEO20: LiTFSI–Li6PS5Cl composite electrolytes with lithium metal”. *ACS applied materials & interfaces* **12**.(10) (2020), pp. 11713–11723. ISSN: 1944-8244. DOI: 10.1021/acsami.9b22968.

[17] Marm B. Dixit et al. “Scalable Manufacturing of Hybrid Solid Electrolytes with Interface Control”. *ACS Applied Materials & Interfaces* **11**.(48) (Dec. 4, 2019). Publisher: American Chemical Society, pp. 45087–45097. ISSN: 1944-8244. DOI: 10.1021/acsami.9b15463.

[18] Trang Thi Vu et al. “Hybrid electrolytes for solid-state lithium batteries: Challenges, progress, and prospects”. *Energy Storage Materials* (2023), p. 102876. ISSN: 2405-8297. DOI: 10.1016/j.ensm.2023.102876.

[19] Yan Ji, Yancheng Zhang, and Chao-Yang Wang. “Li-Ion Cell Operation at Low Temperatures”. *Journal of The Electrochemical Society* **160**.(4) (Feb. 13, 2013). Publisher: IOP Publishing, A636. ISSN: 1945-7111. DOI: 10.1149/2.047304jes.

[20] Zhouyang Jiang et al. “Reducing the Interfacial Resistance in All-Solid-State Lithium Batteries Based on Oxide Ceramic Electrolytes”. *ChemElectroChem* **6**.(12) (June 14, 2019). Publisher: John Wiley & Sons, Ltd, pp. 2970–2983. ISSN: 2196-0216. DOI: 10.1002/celc.201801898.

[21] Sida Huo et al. “Challenges of polymer electrolyte with wide electrochemical window for high energy solid-state lithium batteries”. *InfoMat* **5**.(3) (2023), e12394. ISSN: 2567-3165. DOI: 10.1002/inf2.12394.

[22] *Batteries - European Commission*. URL: https://environment.ec.europa.eu/topics/waste-and-recycling/batteries_en (visited on 03/09/2024).

[23] Hans-Jörg Deiseroth et al. “Li6PS5X: a class of crystalline Li-rich solids with an unusually high Li+ mobility”. *Angewandte Chemie International Edition* **47**.(4) (2008), pp. 755–758. ISSN: 1521-3773. DOI: 10.1002/anie.200703900.

[24] Jae Min Lee et al. “Ionic and electronic conductivities of lithium argyrodite Li6PS5Cl electrolytes prepared via wet milling and post-annealing”. *Frontiers in Chemistry* **9** (2021), p. 778057. ISSN: 2296-2646. DOI: 10.3389/fchem.2021.778057.

[25] Niek JJ De Klerk, Irek Rosłoń, and Marnix Wagemaker. “Diffusion mechanism of Li argyrodite solid electrolytes for Li-ion batteries and prediction of optimized halogen doping: the effect of Li vacancies, halogens, and halogen disorder”. *Chemistry of Materials* **28**.(21) (2016), pp. 7955–7963. ISSN: 0897-4756. DOI: 10.1021/acs.chemmater.6b03630.

[26] William Arnold et al. “Halide doping effect on solvent-synthesized lithium argyrodites Li6PS5X (X= Cl, Br, I) superionic conductors”. *Journal of Power Sources* **464** (2020), p. 228158. ISSN: 0378-7753. DOI: 10.1016/j.jpowsour.2020.228158.

[27] Hirofumi Tsukasaki et al. “Deterioration process of argyrodite solid electrolytes during exposure to humidity-controlled air”. *Journal of Power Sources* **524** (2022), p. 231085. ISSN: 0378-7753. DOI: 10.1016/j.jpowsour.2022.231085.

[28] Zhixia Zhang et al. “Synthesis and characterization of argyrodite solid electrolytes for all-solid-state Li-ion batteries”. *Journal of Alloys and Compounds* **747** (2018), pp. 227–235. ISSN: 0925-8388. DOI: 10.1016/j.jallcom.2018.03.027.

[29] Yizhou Zhu, Xingfeng He, and Yifei Mo. “Origin of outstanding stability in the lithium solid electrolyte materials: insights from thermodynamic analyses based on first-principles calculations”. *ACS applied materials & interfaces* **7**.(42) (2015), pp. 23685–23693. DOI: 10.1021/acsami.5b07517.

[30] Tammo K. Schwietert et al. “Clarifying the relationship between redox activity and electrochemical stability in solid electrolytes”. *Nature Materials* **19**.(4) (Apr. 2020). Publisher: Nature Publishing Group, pp. 428–435. ISSN: 1476-4660. DOI: 10.1038/s41563-019-0576-0.

[31] Darren HS Tan et al. “Elucidating reversible electrochemical redox of Li6PS5Cl solid electrolyte”. *ACS Energy Letters* **4**.(10) (2019), pp. 2418–2427. DOI: 10.1021/acsenergylett.9b01693.

[32] Shuting Luo et al. “Growth of lithium-indium dendrites in all-solid-state lithium-based batteries with sulfide electrolytes”. *Nature Communications* **12**.(1) (2021), p. 6968. ISSN: 2041-1723. DOI: 10.1038/s41467-021-27311-7.

[33] Ajay Gautam et al. “Exploring the Relationship Between Halide Substitution, Structural Disorder, and Lithium Distribution in Lithium Argyrodites (Li6–x PS5–x Br1+ x)”. *Chemistry of Materials* **35**.(19) (2023), pp. 8081–8091. DOI: 10.1021/acs.chemmater.3c01525.

[34] Vasiliki Faka et al. “Pressure dependence of ionic conductivity in site disordered lithium superionic argyrodite Li 6 PS 5 Br”. *Energy Advances* **2**.(11) (2023), pp. 1915–1925. ISSN: 2753-1457. DOI: 10.1039/D3YA00424D.

[35] Zhigang Xue, Dan He, and Xiaolin Xie. “Poly (ethylene oxide)-based electrolytes for lithium-ion batteries”. *Journal of Materials Chemistry A* **3**.(38) (2015), pp. 19218–19253. ISSN: 2050-7496. DOI: 10.1039/C5TA03471J.

[36] A Karmakar and A Ghosh. “A comparison of ion transport in different polyethylene oxide–lithium salt composite electrolytes”. *Journal of Applied Physics* **107**.(10) (2010). ISSN: 0021-8979. DOI: https://doi.org/10.1063/1.3428389.

[37] Władysław Wieczorek et al. “Effect of salt concentration on the conductivity of PEO-based composite polymeric electrolytes”. *The Journal of Physical Chemistry B* **102**.(44) (1998), pp. 8725–8731. ISSN: 1520-6106. DOI: 10.1021/jp982403f.

[38] “Beyond PEO—Alternative host materials for Li+-conducting solid polymer electrolytes”. *Progress in Polymer Science* **81** (2018), pp. 114–143. ISSN: 0079-6700. DOI: 10.1016/j.progpolymsci.2017.12.004.

[39] M Marzantowicz et al. “Crystalline phases, morphology and conductivity of PEO: LiTFSI electrolytes in the eutectic region”. *Journal of power sources* **159**.(1) (2006), pp. 420–430. ISSN: 0378-7753. DOI: 10.1016/j.jpowsour.2006.02.044.

[40] Ludvig Edman, Anders Ferry, and Marca M Doeff. “Slow recrystallization in the polymer electrolyte system poly (ethylene oxide) n–LiN (CF3SO2) 2”. *Journal of Materials Research* **15**.(9) (2000), pp. 1950–1954. ISSN: 2044-5326, 0884-2914. DOI: 10.1557/JMR.2000.0281.

[41] Jiliang Qiu et al. “Enabling stable cycling of 4.2 V high-voltage all-solid-state batteries with PEO-based solid electrolyte”. *Advanced Functional Materials* **30**.(22) (2020), p. 1909392. ISSN: 1616-3028. DOI: 10.1002/adfm.201909392.

[42] Danyang Zhang et al. “Research Progress and Application of PEO-Based Solid State Polymer Composite Electrolytes”. *Frontiers in Energy Research* **9** (Sept. 28, 2021). Publisher: Frontiers. ISSN: 2296-598X. DOI: 10.3389/fenrg.2021.726738.

[43] Jingnan Feng et al. “PEO based polymer-ceramic hybrid solid electrolytes: a review”. *Nano Convergence* **8** (2021), pp. 1–12. ISSN: 2196-5404. DOI: 10.1186/s40580-020-00252-5.

[44] Sanatou Toe et al. “Investigating the Physical State of Polymer Electrolyte: Influence of Temperature and LiTFSI Concentration on the Phase of the Different States of the Polymer Electrolyte PEO-LiTFSI”. *ECS Advances* **2**.(4) (2023), p. 040509. ISSN: 10.1149/2754-2734/ad119d. DOI: 10.1149/2754-2734/ad119d.

[45] A. Vallée, S. Besner, and J. Prud’Homme. “Comparative study of poly(ethylene oxide) electrolytes made with LiN(CF3SO2)2, LiCF3SO3 and LiClO4: Thermal properties and conductivity behaviour”. *Electrochimica Acta* **37**.(9) (Jan. 1, 1992), pp. 1579–1583. ISSN: 0013-4686. DOI: 10.1016/0013-4686(92)80115-3.

[46] M. Marzantowicz et al. “Crystallization and melting of PEO:LiTFSI polymer electrolytes investigated simultaneously by impedance spectroscopy and polarizing microscopy”. *Electrochimica Acta*. Polymer Electrolytes **50**.(19) (June 30, 2005), pp. 3969–3977. ISSN: 0013-4686. DOI: 10.1016/j.electacta.2005.02.053.

[47] Lukas Stolz et al. “Pragmatic Approaches to Correlate between the Physicochemical Properties of a Linear Poly(ethylene oxide)-Based Solid Polymer Electrolyte and the Performance in a High-Voltage Li-Metal Battery”. *The Journal of Physical Chemistry C* **125**.(33) (Aug. 26, 2021). Publisher: American Chemical Society, pp. 18089–18097. ISSN: 1932-7447. DOI: 10.1021/acs.jpcc.1c03614.

[48] *Poly(ethylene oxide) average Mv 300,000, powder 25322-68-3*. URL: http://www.sigmaaldrich.com/ (visited on 10/11/2023).

[49] Qiuju Zheng et al. “Understanding glass through differential scanning calorimetry”. *Chemical reviews* **119**.(13) (2019), pp. 7848–7939. ISSN: 0009-2665. DOI: 10.1021/acs.chemrev.8b00510.

[50] Rivelino VD Montenegro. “Crystallization, biomimetics and semiconducting polymers in confined systems”. PhD thesis. Universität Potsdam, 2003.

[51] Fred A Stevie and Carrie L Donley. “Introduction to x-ray photoelectron spectroscopy”. *Journal of Vacuum Science & Technology A* **38**.(6) (2020). ISSN: 0734-2101. DOI: 10.1116/6.0000412.

[52] Pooja Vadhva et al. “Electrochemical impedance spectroscopy for all-solid-state batteries: Theory, methods and future outlook”. *ChemElectroChem* **8**.(11) (2021), pp. 1930–1947.

[53] RHD Instruments. *RelaxIS*. https://www.rhd-instruments.de/en/. [RelaxIS3]. 2023.

[54] Alexandros Ch Lazanas and Mamas I Prodromidis. "Electrochemical Impedance Spectroscopy— A Tutorial". *ACS Measurement Science Au* (2023). ISSN: 2196-0216. DOI: 10.1002/celc.202100108.

[55] Alma Mathew, Matthew J Lacey, and Daniel Brandell. "Investigating oxidative stability of lithium-ion battery electrolytes using synthetic charge-discharge profile voltammetry". *Journal of Power Sources Advances* **11** (2021), p. 100071. ISSN: 2666-2485. DOI: 10.1016/j.powera.2021.100071.

[56] "Super Soft All-Ethylene Oxide Polymer Electrolyte for Safe All-Solid Lithium Batteries". **6** (). ISSN: 2045-2322. DOI: 10.1038/srep19892.

[57] *Selecting a Sample Pan*. URL: https://folk.ntnu.no/deng/fra_nt/other%20stuff/DSC_manuals/QDSC/Selecting_a_Sample_Pan.htm (visited on 01/10/2024).

A

Supporting Information

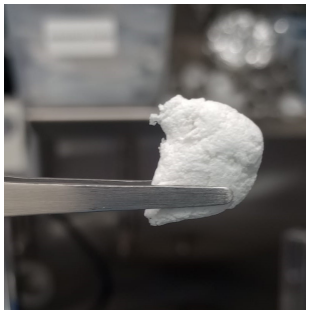

Figure A.1: Dough formation of the mixture of PEO and LiTSFI.

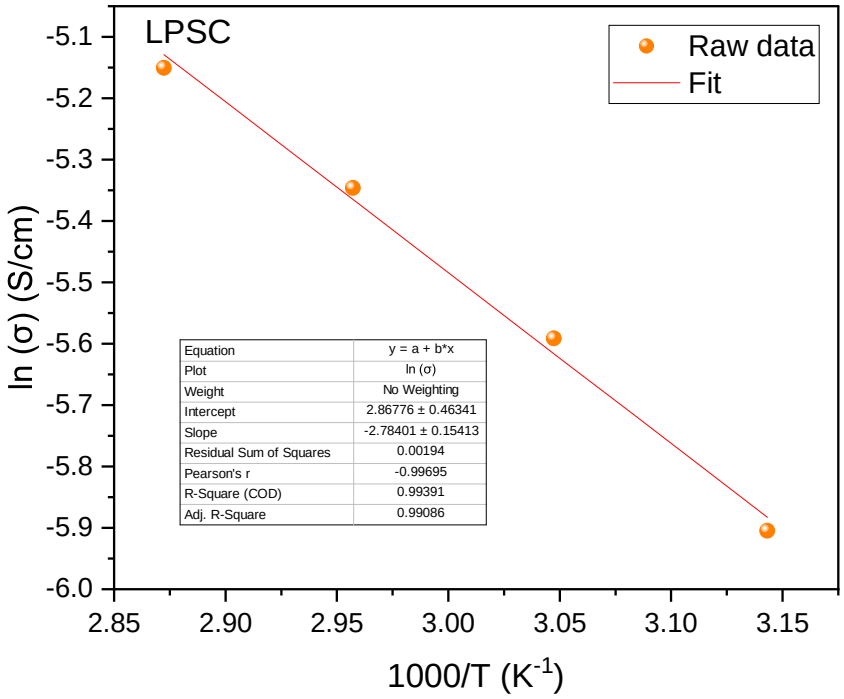

Figure A.2: Arrhenius plot of pristine fine LPSC (NEI Corporation).

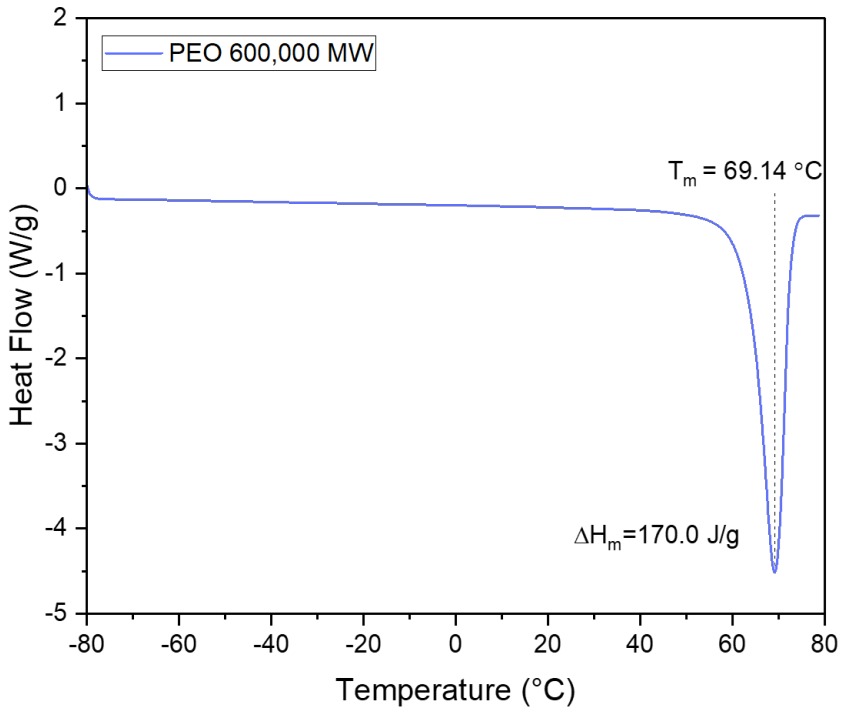

Figure A.3: DSC scan of pristine PEO (Sigma-Aldrich) with a MW of 600,000 g/mol.

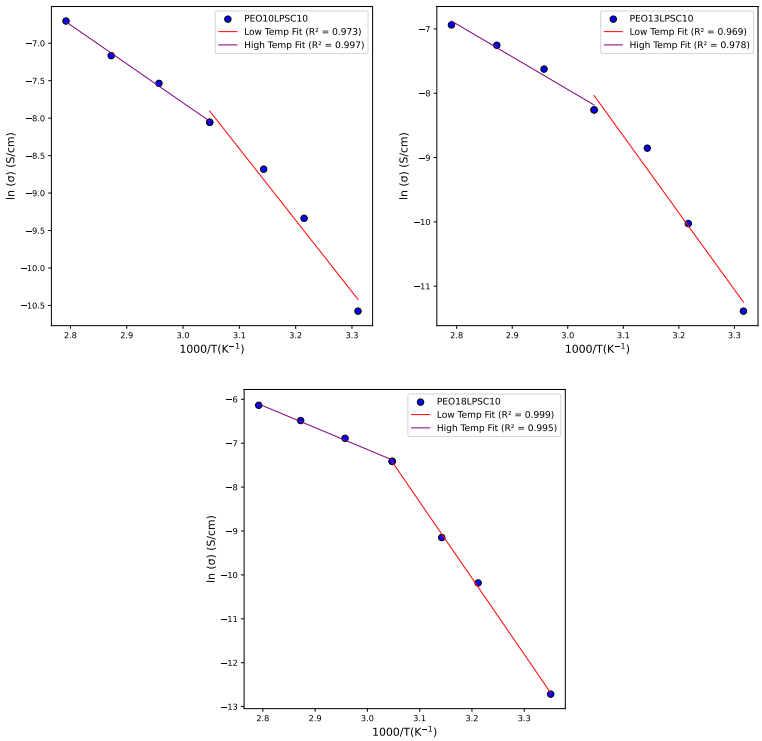

Figure A.4: Fitted Arrhenius plots for 10 wt% LPSC with EO:LI$^+$ ratios 10:1, 13:1 and 18:1 using dry synthesis.

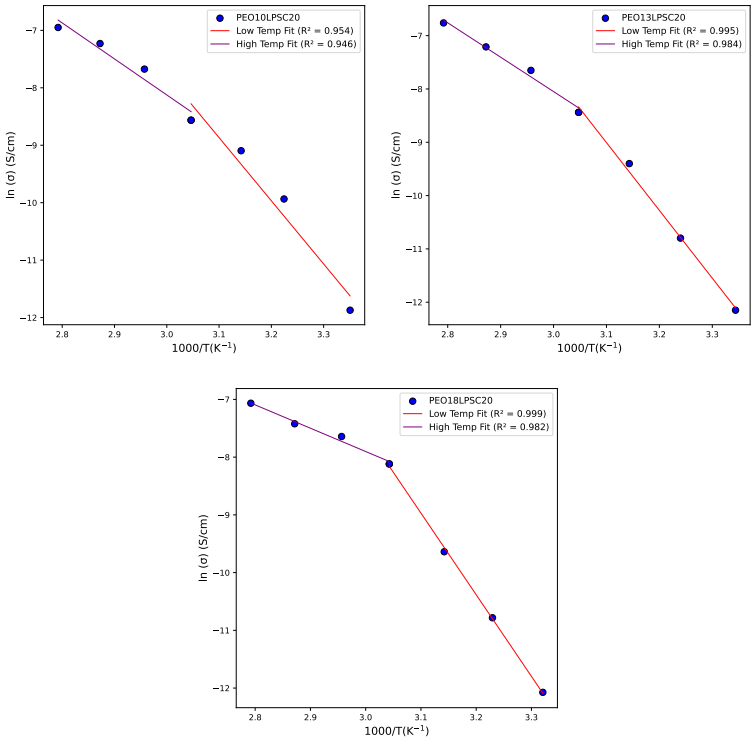

Figure A.5: Fitted Arrhenius plots for 20 wt% LPSC with EO:LI$^+$ ratios 10:1, 13:1 and 18:1 using dry synthesis.

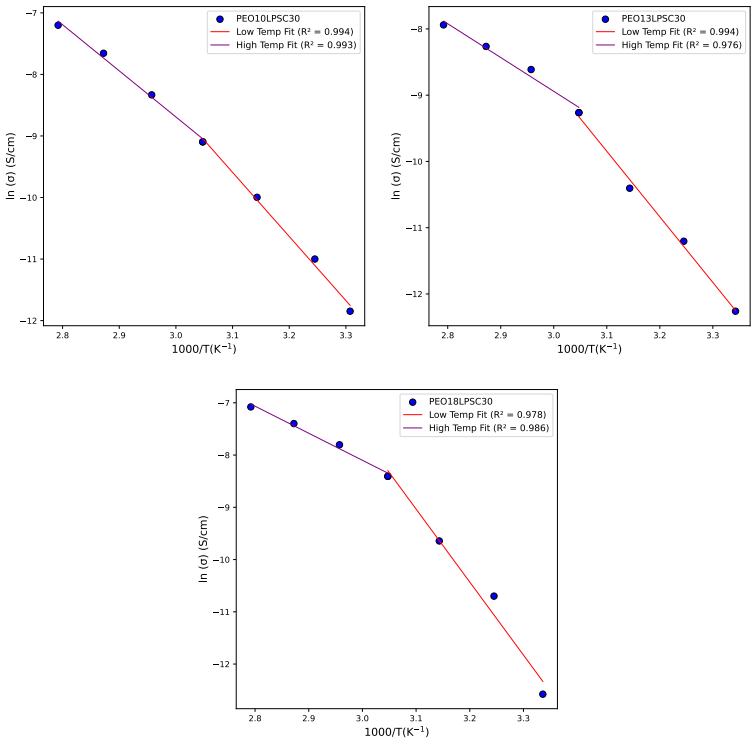

Figure A.6: Fitted Arrhenius plots for 30 wt% LPSC with EO:LI$^+$ ratios 10:1, 13:1 and 18:1 using dry synthesis.

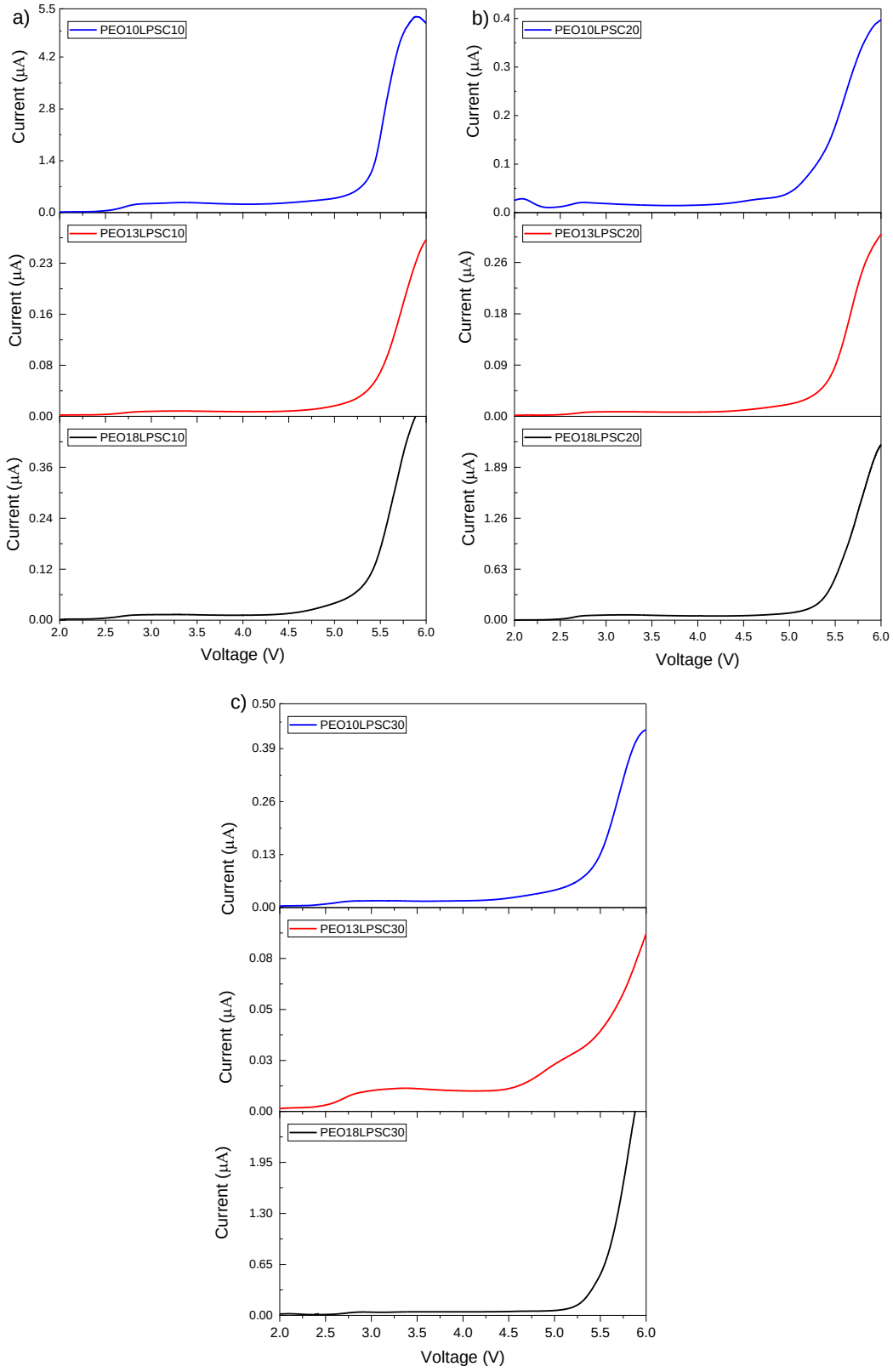

Figure A.7: Anodic scans using LSV for dry syntheis HSE; a) 10 wt% LPSC with EO:LI$^+$ ratios 10:1, 13:1 and 18:1 b) 20 wt% LPSC with EO:LI$^+$ ratios 10:1, 13:1 and 18:1 c) 30 wt% LPSC EO:LI$^+$ ratios 10:1, 13:1.